



Theoretical studies on the electrochemical and mechanical properties and microstructure optimization of micro-tubular solid oxide fuel cells

Jiayu Li ^a, Wei Kong ^a, Zijing Lin ^{a,b,*}

^a Hefei National Laboratory for Physical Sciences at the Microscale and Department of Physics, University of Science and Technology of China, Hefei 230026, China

^b Key Laboratory of Materials Physics, Institute of Solid State Physics, Chinese Academy of Sciences, Hefei 230031, China

HIGHLIGHTS

- A thermal fluid electrochemistry model and a thermal mechanical model are presented.
- Current collection method significantly affects the output of mtSOFC.
- Effects of Ni content on electrochemical and mechanical performance are critically examined.
- Area current outputs of planar and micro-tubular SOFCs are found to be comparable.

ARTICLE INFO

Article history:

Received 15 August 2012

Received in revised form

11 November 2012

Accepted 1 January 2013

Available online 9 January 2013

Keywords:

Thermal fluid model

Electrode composition

Structural mechanics

Thermal stress

Failure analysis

Material design

ABSTRACT

A comprehensive thermal fluid electrochemistry model for the analysis of the electrochemical performance and a thermal mechanical model for the analysis of the mechanical behavior of micro-tubular solid oxide fuel cell (mtSOFC) are presented. Material properties for the models are determined by the available theory and experiment and linked to the compositions and microstructures of the materials. Good agreement between the theoretical and experimental I – V relations is obtained. The mode is used to examine the effects of various parameters on the electrochemical and mechanical performance of mtSOFC. Collecting current from both sides of the anode is found to significantly increase the cell output. Increasing the Ni content or reducing the Ni particle size is generally helpful for improving the electrochemical performance, but the increased Ni content reduces the mechanical stability. The suitable Ni content is thus obtained. The LSM content is inconsequential to the mechanical stability and should be determined by achieving high electrochemical performance. Properly designed mtSOFCs are shown to provide high current outputs. Therefore, mtSOFC is a promising technology with both the benefits of planar SOFC for high current density and tubular SOFC for thermal cycling endurance.

© 2013 Elsevier B.V. All rights reserved.

1. Introduction

Solid oxide fuel cells (SOFCs) are attractive power production devices due to their high energy efficiency and fuel flexibility as well as low pollutant emission [1]. Micro-tubular SOFC (mtSOFC) with tubular diameter under a few millimeters shows high performance on the thermal shock resistance, volumetric power density, fast startup and thermal cycling and has attracted increased attentions [2].

The basic principles governing the choices of SOFC materials have a lot in common for the tubular, planar and micro-tubular

designs. For example, the electrodes should have high conductivities for the charge transport, high catalytic activities for the required chemical and electrochemical reactions, adequate porosity for the gas diffusion, good chemical and mechanical compatibilities with the electrolyte and interconnect materials for the long-term operating stability [3]. Therefore, material compositions and microstructures suitable for tubular SOFCs (tSOFCs) and planar SOFCs (pSOFCs) are often the right choices for mtSOFCs. However, the mtSOFC design has its own distinct characteristics that should be examined to realize its full potential. There is a strong need for in-depth analysis of mtSOFC due to the fact that, as a relatively new design of SOFC, mtSOFC is less studied and understood and there is a large room for its improvement. As the experimental testing is expensive and time consuming, its ability to study the effects of different material parameters and operating conditions on the performance of mtSOFC is severely limited. Mathematical models

* Corresponding author. Hefei National Laboratory for Physical Sciences at the Microscale and Department of Physics, University of Science and Technology of China, Hefei 230026, China. Tel.: +86 551 3606345; fax: +86 551 3606348.

E-mail address: zjlin@ustc.edu.cn (Z. Lin).

incorporating the known physics and behaviors of mtSOFC materials to predict their performance are important tools for the understanding and technological improvement of mtSOFCs.

Numerous mathematical models have been built to study the effect of microstructure on the electrochemical performance [4–12]. De Caluwe et al. [10] developed a one-dimensional button-cell model to examine the influence of anode microstructure on the electrochemical performance. Joan et al. performed numerical analyses on the optimization of cathode microstructures for anode-supported pSOFCs [11]. Several thermal stress models with varying degrees of sophistication [13–24] are also proposed to study the mechanical properties of SOFCs. Yakabe et al. [17–19] evaluated the residual thermal stresses in the electrolyte of anode-supported pSOFCs by a combined experimental and numerical analysis. Selimovic et al. [20] studied the thermal stress of pSOFC in both the steady and transient states. Weil et al. [21] performed a finite element analysis on the magnitudes of thermally induced stress, strain and part deflection in the cell, seal and window frame components under uniform heating and cooling conditions. Nakajo et al. [22,23] used thermo-electrochemical models to study the mechanical issues and the current–voltage (I – V) characterization of pSOFC stacks during assembly, heat-up, dynamic operation, load shutdown and cool-down phases. Recently, Serincan et al. developed a multi-physics model to investigate the effects of different factors on the thermal stresses in a mtSOFC with the thermal expansion coefficients of materials treated as constants [25].

Though there is no shortage of research on the numerical modeling of SOFCs, the theoretical effort focusing on the effects of electrode composition and microstructure on both the electrochemical performance and mechanical property of mtSOFC is relatively rare in the open literature. However, such research effort is quite important for the understanding and development of mtSOFC. For example, a typical mtSOFC consists of a composite anode support, a thin electrolyte layer and a thin composite cathode layer. The composite electrode is a mixture of electron conducting material, such as Ni for the anode or La(Sr)MnO₃ (LSM) for the cathode, and the electrolyte-material, such as yttria-stabilized zirconia (YSZ) [3]. An Ni content close to 40 vol.% in the Ni–YSZ cermet may easily produce an area power density that is higher than its tSOFC counterpart, but substantially lower than that of the pSOFC design [3,26]. Increasing the Ni content to about 50% may significantly increase the power density [3], but the increased Ni content induces mechanical flaw [27]. Therefore, both the electrochemical and mechanical properties and their interplay should be taken into account in order to properly balance their different needs and improve the mtSOFC technology for practical applications.

This work describes a detailed multi-physics model for the numerical simulation of mtSOFCs. The physical properties of composite materials are determined by the available theories and experimental data. The model is used to examine the electrochemical and mechanical performances of mtSOFCs with the representative Ni/YSZ/LSM material set. Effects of the material microstructures such as Ni and LSM contents and their particle sizes on the electrochemical performance and thermal mechanical behavior of mtSOFC are systematically examined. The desirable material compositions and microstructures are thus deduced.

2. Theoretical method

There are two main components in our mathematical model: a thermal fluid electrochemistry model for the analysis of the electrochemical performances and a thermal mechanical model for the analysis of the mechanical behaviors of mtSOFCs. The microstructure based multi-physics electrochemistry model and the structural mechanics model are solved sequentially. The thermal

stress distributions in mtSOFC are evaluated with the temperature fields obtained from the thermal fluid electrochemistry model. The thermal stress distributions and mechanical properties are used by the structural mechanics model to calculate the probability of mechanical failure of the mtSOFC materials. The electrochemistry model and the structural mechanics model may be assembled from various literatures [7,14,28–31]. The precise details of the models used in this work are described in the following.

2.1. Electrochemistry model

The multi-physics electrochemistry model involves coupled electrochemistry, thermal, fluid and electrical transport equations with microstructure-based properties. The basic model parameters for the electrochemical, electrical and thermal properties are determined by the experimental data [32]. The effects of the electrode composition and microstructure on the material properties are considered by the microstructure based effective property theory [33]. Effects of the electrode composition on the electrochemical performance of mtSOFC may then be revealed.

The overall performance of SOFC depends on the operating cell voltage and the output current. The cell operating voltage, V_{cell} , is lower than the open circuit potential (Nernst potential) due to various polarizations such as activation polarization, ohmic polarization and concentration polarization, and may be formally expressed as [30]:

$$V_{\text{cell}} = E_0 - \eta_{\text{ohm}} - \eta_{\text{con}} - \eta_{\text{act}}, \quad (1)$$

where η_{act} is the activation overpotential for the electrochemical reactions, η_{con} is the concentration polarization due to the resistance for the gas transport in porous electrodes, η_{ohm} is the ohmic overpotential and E_0 is the open circuit potential. The open circuit potential of the fuel and oxidant used may be calculated as:

$$E_0 = -\frac{\Delta G^0}{2F} + \frac{RT}{2F} \ln \frac{p_{\text{H}_2}^0 (p_{\text{O}_2}^0)^{0.5}}{p_{\text{H}_2\text{O}}^0}, \quad (2)$$

where ΔG^0 is the free energy change of the reaction $\text{H}_2 + 0.5\text{O}_2 \leftrightarrow \text{H}_2\text{O}$ at the working temperature and when the partial pressures of all the reacting gas species are 1 atm [34].

The concentration polarization (η_{con}) is the sum of the concentration polarizations of anode, $\eta_{\text{con}}^{\text{a}}$, and cathode, $\eta_{\text{con}}^{\text{c}}$. They may be calculated as:

$$\eta_{\text{con}}^{\text{a}} = \frac{RT}{2F} \ln \left(\frac{p_{\text{H}_2}^0 p_{\text{H}_2\text{O}}}{p_{\text{H}_2} p_{\text{H}_2\text{O}}^0} \right), \quad (3)$$

$$\eta_{\text{con}}^{\text{c}} = \frac{RT}{2F} \ln \left(\frac{p_{\text{O}_2}^0}{p_{\text{O}_2}} \right)^{0.5}, \quad (4)$$

where $p_{\text{H}_2}(p_{\text{H}_2\text{O}})$ and $p_{\text{H}_2}^0(p_{\text{H}_2\text{O}}^0)$ denote the partial pressure of H_2 (H_2O) at the anode three phase boundary (TPB) and the anode-fuel channel interface, respectively. p_{O_2} and $p_{\text{O}_2}^0$ are respectively the partial pressure of O_2 at the cathode TPB and the cathode–air channel interface.

The ohmic overpotential includes the electronic and ionic ohmic overpotentials of the anode, cathode and electrolyte and the contact overpotential due to contact ohmic resistance at the interface of different cell components, which may be written as:

$$\eta_{\text{ohm}} = \eta_{\text{ohm}}^{\text{a,e}} + \eta_{\text{ohm}}^{\text{a,i}} + \eta_{\text{ohm}}^{\text{c,e}} + \eta_{\text{ohm}}^{\text{c,i}} + \eta_{\text{ohm}}^{\text{ele,i}} + \eta_{\text{ASR}}. \quad (5)$$

Here $\eta_{\text{ohm}}^{\text{a,e}}$ and $\eta_{\text{ohm}}^{\text{c,e}}$ are the electronic ohmic overpotentials of the anode and the cathode, respectively. $\eta_{\text{ohm}}^{\text{a,i}}$, $\eta_{\text{ohm}}^{\text{c,i}}$ and $\eta_{\text{ohm}}^{\text{ele,i}}$ are

the ionic ohmic overpotentials of the anode, cathode and electrolyte, respectively. η_{ASR} is the contact overpotential and may be calculated as [30]:

$$\eta_{ASR} = j \cdot R_{ASR}, \quad (6)$$

where j is the local current density at the interface and R_{ASR} is the area specific contact resistance.

2.1.1. Governing equations for charge transport

Electronic and ionic current densities in the electrodes and electrolyte are governed by the charge continuity equations and the Ohm's law [7]:

$$\nabla \cdot \vec{i}_{el} = \nabla \cdot \left(-\sigma_{el}^{eff} \nabla \varphi_{el} \right) = \begin{cases} j_{TPB} \lambda_{TPB,eff} & \text{In cathode} \\ -j_{TPB} \lambda_{TPB,eff} & \text{In anode} \end{cases}, \quad (7)$$

$$\nabla \cdot \vec{i}_{io} = \nabla \cdot \left(-\sigma_{io}^{eff} \nabla \varphi_{io} \right) = \begin{cases} -j_{TPB} \lambda_{TPB,eff} & \text{In cathode} \\ 0 & \text{In electrolyte} \\ j_{TPB} \lambda_{TPB,eff} & \text{In anode} \end{cases} \quad (8)$$

where \vec{i}_{el} (\vec{i}_{io}) is the vector of electronic (ionic) current density, σ_{el}^{eff} (σ_{io}^{eff}) is the effective electronic (ionic) conductivity, and φ_{el} (φ_{io}) is the local electronic (ionic) potential. $\lambda_{TPB,eff}$ is the effective volume specific TPB length. j_{TPB} is the TPB length specific transfer current density and is defined as positive when the current flows from the ionic phase to the electronic phase. j_{TPB} is a nonlinear function of the local activation polarization, η_{act} , i.e., the voltage sacrificed to overcome the activation barriers associated with the electrochemical reaction. The relationship between j_{TPB} and η_{act} may be described by the Butler–Volmer equation [35]:

$$j_{TPB} = j_0 \left[\exp \left(\frac{2\alpha_f F}{RT} \eta_{act} \right) - \exp \left(-\frac{2\beta_f F}{RT} \eta_{act} \right) \right], \quad (9)$$

where α_f (β_f) is the forward (reverse) reaction symmetric factor. j_0 is the local exchange transfer current per unit TPB length which is estimated as [36]:

$$j_0^c = j_{0,ref}^c \exp \left(-\frac{E_{O_2}}{R} \left(\frac{1}{T} - \frac{1}{T_{ref}} \right) \right) \left(\frac{p_{O_2}}{p_{O_2}^0} \right)^{0.25} \quad (10)$$

$$j_0^a = j_{0,ref}^a \exp \left(-\frac{E_{H_2}}{R} \left(\frac{1}{T} - \frac{1}{T_{ref}} \right) \right) \left(\frac{p_{H_2} p_{H_2O}}{p_{H_2}^0 p_{H_2O}^0} \right) \quad (11)$$

where T is the temperature and R is the universal gas constant. $j_{0,ref}^a$ ($j_{0,ref}^c$) is the anode (cathode) exchange transfer current density at the reference temperature, T_{ref} , and is treated as an adjustable parameter for fitting the experimental result. E_{H_2} (E_{O_2}) is the activation energy for the anode (cathode) electrochemical reaction.

The anode and cathode activation polarizations, η_{act}^a and η_{act}^c , for Eq. (9) may be expressed as,

$$\eta_{act}^a = \varphi_{el} - \varphi_{io} - \eta_{con}^a, \quad (12)$$

$$\eta_{act}^c = \varphi_{io} - \varphi_{el} - \eta_{con}^c. \quad (13)$$

The ohmic overpotentials in Eq. (5), $\eta_{ohm}^{a,e}$, $\eta_{ohm}^{c,e}$, $\eta_{ohm}^{a,i}$, $\eta_{ohm}^{c,i}$ and $\eta_{ohm}^{ele,i}$, are determined by the electronic (ionic) potential differences along the electronic (ionic) current flux paths.

2.1.2. Effective conductivities and effective TPB length

The effective conductivity of the k -phase material (electronic or ionic conducting material) may be calculated by [37]:

$$\sigma_k^{eff} = \sigma_k^0 \left(\frac{\psi_k - \psi_k^t}{1 + \phi_g / (1 - \phi_g) - \psi_k} \right)^2, \quad (14)$$

where ϕ_g is the porosity ratio, ψ_k and ψ_k^t are respectively the volume fraction and the percolated volume fraction threshold of the k -phase material. Eq. (14) applies only for $\psi_k > \psi_k^t$. σ_k^{eff} is set to zero when $\psi_k < \psi_k^t$. ψ_k^t is calculated as [38],

$$\bar{Z} \frac{\psi_k^t / r_k}{\psi_k^t / r_k + (1 - \psi_k^t) / r_l} = 1.764, \quad (15)$$

where r_i ($i = k, l$) is the radius of i -phase particle, \bar{Z} is the average coordination number of all solid particles and set to 6 [38,39].

The intrinsic conductivities (σ_k^0) of Ni, LSM and YSZ are determined as [7,40],

$$\sigma_{Ni}^0 = 3.27 \times 10^6 - 1065.3T, \quad (16)$$

$$\sigma_{LSM}^0 = \frac{4.2 \times 10^7}{T} \exp \left(\frac{-1150}{T} \right), \quad (17)$$

$$\sigma_{YSZ}^0 = 6.25 \times 10^4 \exp \left(\frac{-10300}{T} \right). \quad (18)$$

The effective or percolated volume specific TPB length is determined as:

$$\lambda_{TPB,eff}^v = 2\pi \min(r_{ed}, r_{el}) (\sin \theta) n_k^V Z_{ed,el} P_{ed} P_{el}, \quad (19)$$

where $n_k^V = 3(1 - \phi_g)\psi_k / 4\pi r_k^3$ [7] is the volumetric number density of k particles in a composite electrode, θ is the angle of particle contact (assumed to be 15° [38]). $Z_{k,l}$ is the average number of k -particles in contact with a l -particle that may be estimated as [33]:

$$Z_{k,l} = 0.5 \left(1 + r_k^2 / r_l^2 \right) \bar{Z} \frac{\psi_l / r_l}{\sum_{k=1}^M \psi_k / r_k}. \quad (20)$$

The percolation probability of the electrode (electrolyte) particles, P_{ed} (P_{el}), can be calculated as [38]:

$$P_k = \left(1 - \left(\frac{3.764 - Z_{k,k}}{2} \right)^{2.5} \right)^{0.4}. \quad (21)$$

2.2. Thermal fluid model

2.2.1. Mass transport equations

This model describes an mtSOFC unit running on hydrogen and air. The humidified hydrogen gas is supplied as fuel in the anode. Air is supplied as oxidant, consisting of two components: oxygen and nitrogen.

The mass transport in the gas channel may be described by the mass balance equation:

$$\nabla \cdot \vec{N}_i = \nabla \cdot \left(-D_i \nabla C_i + C_i \vec{u} \right) = R_i \quad (22)$$

where \vec{N}_i is the molar flux of species i , C_i the molar concentration of species i , \vec{u} the vector of convection velocity. R_i is the reaction rate

of species i and is zero in the gas channel. D_i , the diffusion coefficient of species i , is the same as the binary diffusion coefficient D_{ij} as the fuel and air each consists of only two species. The binary diffusion coefficient D_{ij} may be evaluated as [31],

$$D_{ij} = \frac{3.198 \times 10^{-8} T^{1.75}}{p(v_i^{1/3} + v_j^{1/3})} \left(\frac{1}{M_i} + \frac{1}{M_j} \right)^{0.5}, \quad (23)$$

where p is the gas pressure, v is the diffusion volume (6.12×10^{-6} , 13.1×10^{-6} , 16.3×10^{-6} and $18.5 \times 10^{-6} \text{ m}^3 \text{ mol}^{-1}$ for H_2 , H_2O , O_2 and N_2 , respectively [41]), M is the molecular mass and the subscript i (j) refers to the gas species i (j).

The mass transport in the porous electrodes also obeys the mass balance equation, $\nabla \cdot \vec{N}_i = R_i$. The rates of hydrogen, oxygen and steam productions are calculated respectively as:

$$R_{\text{H}_2} = -\frac{i_e}{2F}, \quad (25)$$

$$R_{\text{O}_2} = -\frac{i_e}{4F}, \quad (26)$$

$$R_{\text{H}_2\text{O}} = \frac{i_e}{2F}, \quad (27)$$

where $i_e = j_{\text{TPB}} \lambda_{\text{TPB,eff}}$ is the current density. The molar fluxes of gas species in the porous electrodes should be described by the dusty gas model that takes the Knudsen diffusion into account [42]. For binary flow, the molar flux may be written as [43]:

$$N_i = N_i^{\text{diffusion}} + N_i^{\text{convection}} = -D_i \nabla C_i - C_i \frac{\bar{B}}{\mu} \nabla p \quad (28)$$

where

$$D_i = \frac{D_{12}^{\text{eff}} D_{iK}^{\text{eff}}}{D_{12}^{\text{eff}} + x_1 D_{2K}^{\text{eff}} + x_2 D_{1K}^{\text{eff}}} \quad (29-1)$$

$$\bar{B} = B_0 + \frac{D_{1K}^{\text{eff}} D_{2K}^{\text{eff}}}{\text{RTC}_{\text{tot}} (D_{12}^{\text{eff}} + x_1 D_{2K}^{\text{eff}} + x_2 D_{1K}^{\text{eff}})}. \quad (29-2)$$

Here x_i is the molar fraction of species i , B_0 is the permittivity, D_{ij}^{eff} and D_{iK}^{eff} are respectively the effective binary diffusion coefficient and effective Knudsen diffusion coefficient of species i . C_{tot} is the total molar concentration of species in the electrode. μ is the effective viscosity coefficient of the mixture fluid that may be calculated as [35]:

$$\mu = \sum_{i=1}^m \frac{x_i / \mu_i}{\sum_{j=1}^m x_j \phi_{ij}}, \quad (30)$$

where m is the number of component in the fluid and ϕ_{ij} is a dimensionless number determined by:

$$\phi_{ij} = \frac{1}{\sqrt{8}} \left(1 + \frac{M_i}{M_j} \right)^{-0.5} \left[1 + \left(\frac{\mu_i}{\mu_j} \right)^{0.5} \left(\frac{M_i}{M_j} \right)^{0.25} \right]^2. \quad (31)$$

Here μ_i (μ_j) is the viscosity coefficient of species i (j), which may be obtained from the Sutherland law [44]:

$$\mu_i = \mu_{\text{ref}} \frac{T_{\text{ref}} + c_{\text{ref}}}{T + c_{\text{ref}}} \left(\frac{T}{T_{\text{ref}}} \right)^{1.5}, \quad (32)$$

where μ_{ref} is the reference viscosity at the reference temperature, T_{ref} , and c_{ref} is the Sutherland's constant.

B_0 , D_{ij}^{eff} and D_{iK}^{eff} are calculated by the following equations [45,46]:

$$B_0 = \frac{\phi_g^3}{45(1 - \phi_g)^2} r_{\text{el}}^2, \quad (33)$$

$$D_{ij}^{\text{eff}} = \frac{\epsilon}{\tau} D_{ij}, \quad (34)$$

$$D_{iK}^{\text{eff}} = \frac{\epsilon}{\tau} D_{iK} = \frac{2\epsilon}{3\tau} r_g \sqrt{\frac{8RT}{\pi M_i}}, \quad (35)$$

where ϵ is the porosity, τ is the tortuosity factor and r_g is the pore radius determined as [33]

$$r_g = \frac{2}{3} \frac{1}{1 - \phi_g} \frac{1}{\psi_{\text{ed}}/r_{\text{ed}} + \psi_{\text{el}}/r_{\text{el}}}. \quad (36)$$

2.2.2. Momentum transport

The momentum transport in the fuel channel is described by the Navier–Stokes equation:

$$\nabla \cdot (\mu (\nabla \vec{u} + (\nabla \vec{u})^T)) - \nabla p = \rho (\vec{u} \cdot \nabla) \vec{u}, \quad (37)$$

$$\nabla \cdot \vec{u} = 0. \quad (38)$$

Here ρ is the gas density given by:

$$\rho = \frac{p}{RT} \left(\sum_i x_i M_i \right). \quad (39)$$

The momentum transport in the porous electrodes is modeled by the Brinkman equation that accounts for the viscous transport in the momentum balance and treats both the pressure and the flow velocity vector as independent variables [47]:

$$\frac{\mu}{B_0} \vec{u} = -\nabla p + \nabla \cdot \left(\frac{\mu}{\phi_g} (\nabla \vec{u} + (\nabla \vec{u})^T) \right) - \nabla \cdot \left(\frac{2\mu}{3\phi_g} \nabla \cdot \vec{u} I \right). \quad (40)$$

2.2.3. Heat transport

The energy conservation equation in this model is written as:

$$\nabla \cdot (-k^{\text{eff}} \nabla T) + \rho C_p \vec{u} \cdot \nabla T = Q, \quad (41)$$

where Q is the heat source that includes the Ohmic heat source, Q_{ohm} , activation heat source, Q_{act} , and the entropy heat source, Q_{entr} . The heat sources may be expressed as:

$$Q_{\text{ohm}} = \frac{i_{\text{el}}^2}{\sigma_{\text{el}}} + \frac{i_{\text{io}}^2}{\sigma_{\text{io}}} \quad (42)$$

$$Q_{\text{act}} = i_{\text{el}} \eta_{\text{act}}, \quad (43)$$

$$Q_{\text{entr}} = i_{\text{el}} \left(\frac{-T \Delta S}{2F} \right). \quad (44)$$

k_{eff} in Eq. (41) is the effective thermal conductivity of the porous material and determined as:

$$k_{\text{eff}} = \phi_g k_f + (1 - \phi_g) k_s, \quad (45)$$

where k_s is the thermal conductivity of the solid material and k_f is the effective thermal conductivity of the fluid that is calculated as [41]:

$$k_f = \sum_{i=1}^n \frac{x_i k_i}{\sum_{j=1}^n x_j A_{ij}}, \quad (46)$$

where A_{ij} is evaluated by [41],

$$A_{ij} = \left(1 + \left(\frac{u_i}{u_j} \right)^{0.5} \left(\frac{M_j}{M_i} \right)^{0.25} \right)^2 \times \left(8 \left(1 + \frac{M_i}{M_j} \right) \right)^{-0.5}. \quad (47)$$

k_i in Eq. (46) is the thermal conductivity of species i and determined as [41]:

$$k_i = b_i^1 \times 10^{-2} + b_i^2 \times 10^{-5}T + b_i^3 \times 10^{-8}T^2. \quad (48)$$

The required parameters, b_i^1 , b_i^2 and b_i^3 , are obtained by fitting the experimental results [48] and are listed in Table 1.

C_p in Eq. (41) is the effective specific heat of the fluid and evaluated as [41]:

$$C_p = \sum_i x_i C_p^i, \quad (49)$$

where C_p^i is the specific heat of species i and calculated as [41]:

$$C_p^i = a_i^1 + a_i^2 \times 10^{-3}T + a_i^3 \times 10^{-6}T^2. \quad (50)$$

The required parameters, a_i^1 , a_i^2 and a_i^3 , are obtained by fitting the experimental data [48] and listed in Table 1.

At the interface between the air flow and the mtSOFC cathode, the heat transport due to the convective heat transfer and radiation should be considered. The convective heat transfer between the air and the cathode outer surface may be described with the Newton's law of cooling:

$$Q_{\text{con}} = h(T_{\text{ext}} - T), \quad (51)$$

where T_{ext} is the external temperature of air, or the temperature of the furnace wall in this study. h is the heat transfer coefficient estimated as [29]:

$$h = \frac{N_u k_i}{d}, \quad (52)$$

where d is the hydraulic diameter and N_u is the Nusselt number calculated as [48]:

$$N_u = 3.66 + \frac{0.0668(d/l)Re Pr}{1 + 0.04((d/l)Re Pr)^{2/3}}. \quad (53)$$

Here Pr is the Prandtl number, Re is the Reynolds number and l is the length of the mtSOFC tube.

The radiative heat transfer between the cathode outer surface and the furnace wall may be calculated as:

$$Q_{\text{rad}} = \epsilon_{\text{rad}} (T_{\text{fw}}^4 - T^4), \quad (54)$$

where T_{fw} is the temperature of the furnace wall. ϵ_{rad} is the surface emissivity of the cathode.

Combining both convective heat transfer and radiation, the heat transport at the interface between the air flow and the mtSOFC cathode is described by:

$$-\vec{n} \cdot (-k \nabla T + \rho C_p \vec{u} T) = h(T_{\text{ext}} - T) + \epsilon_{\text{rad}} (T_{\text{fw}}^4 - T^4). \quad (55)$$

To be precise, the material properties and operating parameters used in this study are listed in Table 2.

2.3. Structural mechanics model

This study focuses on both the residual stress determined by the material manufacturing process and material properties and the operating thermal stress based on the temperature profile obtained

Table 2

Fuel cell material properties and operating parameters.

Fuel flow rate (u_0)	1.06 m s ⁻² [26]
Fuel or air pressure (P_0)	101,325 Pa [26]
Operating temperature (T_{op})	1073 K [26]
Operating voltage (V_{cell})	0.7 V
Molar air composition	21% O ₂ and 79% N ₂ [26]
Molar fuel composition	97% H ₂ and 3% H ₂ O [26]
Tortuosity (τ)	3 [7]
Thermal conductivity of anode	2 W m ⁻² s ⁻¹ [49,50]
Thermal conductivity of YSZ	2 W m ⁻² s ⁻¹ [49,50]
Thermal conductivity of LSM	4 W m ⁻² s ⁻¹ [49,50]
Activation energies for the anode (E_{H_2})	120 kJ mol ⁻¹ [36]
Activation energies for the cathode (E_{O_2})	130 kJ mol ⁻¹ [36]
Forward reaction symmetric factor for anode (α_f)	1.5 [7]
Reverse reaction symmetric factor for anode (β_f)	0.5 [7]
Forward reaction symmetric factor for cathode (α_f)	0.65 [7]
Forward reaction symmetric factor for cathode (β_f)	0.35 [7]
Exchange transfer current density of anode ($j_{0,\text{ref}}^a$)	8 × 10 ⁻³ A m ⁻¹ [7]
Exchange transfer current density of cathode ($j_{0,\text{ref}}^c$)	1.25 × 10 ⁻⁴ A m ⁻¹ [7]
Ni radius (r_{Ni})	0.33 × 10 ⁻⁶ m
YSZ radius (r_{YSZ})	0.3 × 10 ⁻⁶ m
LSM radius (r_{LSM})	0.3 × 10 ⁻⁶ m
Volume fraction of Ni (ψ_{Ni})	0.445 [26]
Volume fraction of LSM (ψ_{LSM})	0.479 [26]
Porosity of anode (φ_g)	0.4
Porosity of cathode (φ_g)	0.4
Prandtl number for air (Pr)	0.7 [51]
Thermal surface emissivity (ϵ_{rad})	0.3 [52]
Anode length	30 × 10 ⁻³ m [26]
Cathode length	11.8 × 10 ⁻³ m [26]
Electrolyte length	20 × 10 ⁻³ m [26]
Width of anode current collector	5 × 10 ⁻³ m [26]
Anode thickness	0.15 × 10 ⁻³ m [26]
Cathode thickness	20 × 10 ⁻⁶ m [26]
Electrolyte thickness	12 × 10 ⁻⁶ m [26]
Tubular interior diameter	0.85 × 10 ⁻³ m [26]
Furnace interior diameter	6 × 10 ⁻³ m [26]
Anode and electrolyte stress free temperature	1473 K [15]
Cathode stress free temperature	1373 K [70]

Table 1

Parameters for calculating the viscosities, specific heats and thermal conductivities of gas species [48].

Gas	For viscosity			For specific heat			For thermal conductivity		
	μ_{ref} (Pa·s)	T_{ref}	c_{ref}	a_i^1	a_i^2	a_i^3	b_i^1	b_i^2	b_i^3
H ₂	8.41×10^{-6}	273 K	96.7 K	29.09	0.836	-0.327	5.61	39.36	61.7
H ₂ O	1.70×10^{-6}	273 K	861 K	30.0	10.7	-2.02	-0.27	6.64	1.38
O ₂	19.2×10^{-6}	273 K	139 K	36.16	0.845	-0.749	0.21	8.31	-1.41
N ₂	16.6×10^{-6}	273 K	107 K	27.32	6.23	-0.950	1.77	4.22	0.506

from the above described thermal-fluid electrochemical model. Thermal stress was calculated using the solid mechanics model. It is assumed that all the materials of the SOFC undergo elastic deformation when subject to thermal loads. In this model, no shrinkage is considered during the reduction of NiO into Ni and the coefficients of thermal expansion (CTEs) of NiO/YSZ and Ni/YSZ are considered to be equal. This model is often used in the open literature [53] and adopted to calculate the stress distribution of the Ni/YSZ anode in the work.

2.3.1. The stress–strain relation

In the solid mechanics model, the stress–strain constitutive relation may be written as,

$$\sigma = D\xi_{\text{el}} + \sigma_0, \quad (56)$$

where σ is the stress tensor, D is the elasticity matrix, ξ_{el} is the elastic strain, σ_0 is the initial stress or the residual stress. In this work, the gravitational forces are assumed to have a negligible contribution to the overall stress distribution and the materials undergo free deformations.

For an isotropic material in axial symmetry, D is defined as [14]:

$$D = \frac{E}{(1+v)(1-2v)} \begin{bmatrix} 1-v & v & v & 0 \\ v & 1-v & v & 0 \\ v & v & 1-v & 0 \\ 0 & 0 & 0 & \frac{1-2v}{2} \end{bmatrix}, \quad (57)$$

where E is the Young's modulus and v is the Poisson's ratio of the material defined by:

$$v = \frac{E}{2G} - 1, \quad (58)$$

where G is the shear modulus of the material.

The elastic strain, ξ_{el} , is a component of the total strain, ξ , that also includes the thermal strain, ξ_{th} , and the initial strain, ξ_0 ,

$$\xi = \xi_{\text{el}} + \xi_{\text{th}} + \xi_0. \quad (59)$$

The thermal strain may be calculated as,

$$\xi_{\text{th}} = \alpha(T - T_f), \quad (60)$$

where α is for the CTE of the material, T is the local temperature obtained from the thermal-fluid model, and T_f is the stress free temperature at which there is no stress accumulated in the material.

Combining Eq. (59) and Eq. (60) and considering the relationship between the initial strain and initial stress, $\sigma_0 = D\xi_0$, Eq. (56) may be rewritten as,

$$\sigma = D(\xi - \xi_{\text{th}} - \xi_0) + \sigma_0 = D[\xi - \alpha(T - T_f)]. \quad (56a)$$

2.3.2. Material properties

For the mtSOFC studied here, YSZ electrolyte is coated on porous Ni-YSZ anode and LSM–YSZ is used as cathode. Mechanical properties for the dense anode and cathode are calculated using the relations given for heterogeneous materials based on the “composite sphere method” (CSM) [54]:

$$K_{\text{com}} = K_2 + \frac{\psi_1}{1/(K_1 - K_2) + 3\psi_2/(3K_2 + 4G_2)}, \quad (61)$$

$$G_{\text{com}} = G_2 + \frac{\psi_1}{1/(G_1 - G_2) + 6\psi_2(3K_2 + 2G_2)/(5G_2(3K_2 + 4G_2))}. \quad (62)$$

Here K_{com} and G_{com} are the bulk modulus and shear modulus of the dense composite material, respectively. K_2 (K_1) and G_2 (G_1) are respectively the bulk and shear modulus of the matrix (impurity) in the composite material.

The effective elastic and shear modulus for the porous material are given by the approach developed by Ramakrishnan and Arunachalam [55], effective Young's modulus E_{eff} and shear modulus G_{eff} are determined as:

$$E_{\text{eff}} = E_0 \frac{(1 - \phi_g)^2}{1 + (2 - 3v_0)\phi_g}, \quad (63)$$

$$G_{\text{eff}} = G_0 \frac{(1 - \phi_g)^2}{1 + (11 - 19v_0)/(4 - 4v_0)\phi_g}, \quad (64)$$

where the subscript “0” refers to the property of the dense material. Inserting Eqs. (63) and (64) into Eq. (58), the effective Poisson ratio, v_{eff} , for the porous material may be calculated as:

$$v_{\text{eff}} = \frac{1}{4} \frac{4v_0 + 3\phi_g - 7v_0\phi_g}{1 + 2\phi_g - 3v_0\phi_g}. \quad (65)$$

The effective CTE of the composite electrode may be calculated as [56]:

$$\alpha_{\text{com}} = \frac{\alpha_1\psi_1 K_1 + \alpha_2\psi_2 K_2}{\psi_1 K_1 + \psi_2 K_2}. \quad (66)$$

The effect of porosity on CTE is neglected as studies have shown that there is no significant influence of porosity on the thermal expansion [57,58]. The mechanical properties of the dense materials are shown in Table 3.

2.4. Failure probability analysis

The mechanical failure in a ceramic component occurs due to the brittle nature of the material. Meanwhile, the ceramics exhibit a statistical strength distribution [52]. Therefore, analyzing the failure probability of the ceramic component is necessary. The Weibull approach of failure analysis is adopted here to estimate the risk flaws of the ceramic component. The Weibull method [65] calculates the failure probability, P_f , of the ceramic component with the magnitude of the tensile stress, σ_{ten} :

$$P_f = 1 - \exp\left(-\int_V \left(\frac{\sigma_{\text{ten}}}{\sigma_0}\right)^m \frac{dV}{V_0}\right), \quad (67)$$

where σ_0 is the Weibull strength at the reference volume, V_0 , V is the volume of the ceramic component and m represents the Weibull modulus which corresponds to a shape parameter. For

Table 3
Mechanical properties of dense materials.

Material	Young' modulus (GPa)	Poisson ratio	CTE (10^{-6} K^{-1})	Density (10^3 kg m^{-3})
YSZ	215 [13]	0.317 [13]	10.3 [59]	6.04 [60]
YSZ (800 °C)	185 [13]			
Ni	200 [61]	0.313 [14]	16.9 [59]	8.9 [14]
Ni (800 °C)	171 [62]			
LSM	95 [63]	0.32 [14]	12.4 [64]	6.57 [60]

a material subjecting to a multi-axial stress, the total survival probability may be calculated as the product of the survival probabilities determined by the three principal stresses, σ_i . As a result, the total failure probability is calculated as:

$$P_f^m = 1 - \prod_{i=1}^3 \exp \left(- \int_V \left(\frac{\sigma_i}{\sigma_0} \right)^m \frac{dV}{V_0} \right). \quad (68)$$

The three principal stresses, σ_1 , σ_2 and σ_3 , are the components of the stress tensor when the basis is changed in such a way that the shear stress components become zero. Moreover, the principal stresses are chosen such that $\sigma_1 > \sigma_2 > \sigma_3$. The stress is tensile if $\sigma_i > 0$, and the stress is compressive if $\sigma_i < 0$. The Weibull analysis only applies for a tensile stress. $\sigma_i = 0$ is used in calculating Eq. (68) where a compressive stress ($\sigma_i < 0$) is encountered in the stress field. The Weibull parameters for the SOFC materials studied here are shown in Table 4 [13,53,66].

When subjecting to a compressive stress, the material survives if the stress is below its compressive strength. Otherwise, the material fails mechanically. The compressive strengths of the YSZ electrolyte and the LSM–YSZ composite cathode are listed in Table 5.

3. Numerical method

3.1. Geometric model

Fig. 1a shows an anode-supported mtSOFC. The inner layer is the porous anode where fuel flows through the cell tube. The outer layer is the porous cathode where air flows around. The middle layer is the dense YSZ electrolyte that conducts oxygen ions but not the electrons. There is an axial symmetry in the mtSOFC and the numerical model is two dimensional (2D) in nature. The 2D computational domain is illustrated in Fig. 1b. The actual three dimensional geometry of the mtSOFC may be obtained by revolving the computational domain around the symmetry axis.

3.2. Boundary conditions

The boundary conditions are critically important for the solutions of the above described partial differential equations (PDEs) for the thermal fluid electrochemistry model and the structural mechanics model and should be specified for all relevant boundaries. Table 6 summarizes the boundary settings for the multi-physics electrochemistry model. The boundary conditions for the structural mechanics are set to be free deformation.

3.3. Numerical solution

The PDEs for the thermal fluid electrochemistry model and the structural mechanics model with the appropriate boundary conditions were solved using the finite element commercial software COMSOL MULIPHYSICS Version 3.5a [47]. The COMSOL stationary

Table 4
Weibull parameters for SOFC material used in this model [13,54,67].

Material	Weibull modulus, m	Weibull strength, σ_0 (MPa)	Reference volume, V_0 (10^{-9} m^3)
Anode (298 K)	11.8	187	0.578
Anode (1073 K)	6.1	115	1.0 ^a
Electrolyte (298 K)	7.0	446	0.35
Electrolyte (1073 K)	8.0	282	0.270
LSM (298 K)	7.0	52	1.210
LSM (1073 K)	4.0	75	2.810

^a Assumed.

Table 5
Compressive strength.

Material	Room temperature	Operating temperature
Electrolyte	1 GPa [67]	235 MPa [68]
Cathode	100 MPa [69]	23.5 MPa ^a

^a Assumed.

nonlinear solver uses an affine invariant form of the damped Newton method to solve the discretized PDEs with a relative convergence tolerance of 1.0×10^{-6} . The two sets of PDEs for the multi-physics electrochemistry model and the structural mechanics model are solved sequentially: the thermal fluid electrochemistry model is solved first and then the predicted temperature field is used in the solid mechanics model. Unless explicitly stated otherwise, the standard parameter sets shown in Tables 1–6 are used as the defaults in the numerical simulations throughout this work.

4. Results and discussion

4.1. Performance of mtSOFC with the default material parameters

4.1.1. Validation of the numerical model

An mtSOFC with Ni–YSZ composite anode, YSZ electrolyte and LSM–YSZ cathode was manufactured and its I – V relations were measured at the temperatures of 600, 700 and 800 °C [26]. In the experiment, the current was collected only from one side of the anode layer, instead of from both sides of the anode tube as indicated in Fig. 1. For comparison, the numerical model also used the one-side anode current collection mode. The parameters shown in Tables 1–5 were used. Most of these parameters were obtained by previous experimental measurements on pSOFCs [32] or deduced

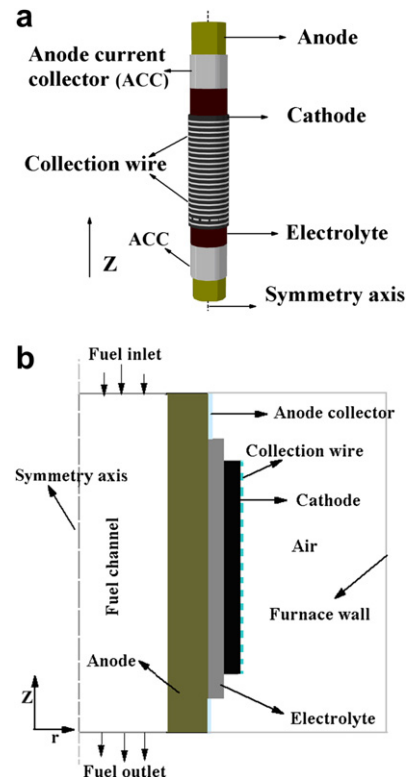


Fig. 1. Schematic of mtSOFC (a) three-dimensional structure, (b) two-dimensional computational domain.

Table 6

Boundary conditions for the thermal fluid electrochemistry model.

Boundary	Charge transport	Mass transport	Momentum transport	Heat transport
Fuel channel inlet		H ₂ and H ₂ O concentration	Laminar flow (u_0)	Temperature (T_{op})
Fuel channel outlet		Convective flux	Pressure, no viscous stress (P_0)	Convective flux
Interconnect–anode interface	Reference potential (E_0)	Insulation	No slip	Heat flux (Eq. (55))
Air channel–Cathode interface	Reference potential (V_{cell})	O ₂ and N ₂ concentration		Heat flux (Eq. (55))
Air channel–electrolyte interface	Electric insulation	Insulation		Heat flux (Eq. (55))
Fuel channel – Anode interface	Electric insulation	Continuous	Continuous	Continuous
Electrolyte–anode interface	Electric insulation	Insulation	No slip	Continuous
Electrolyte–cathode interface	Electric insulation	Insulation		Continuous
All others	Electric insulation	Insulation	No slip	Adiabatic

from fitting the experiments [7,32]. The main changes concern the particle sizes of the electrode materials. There are both Ni–YSZ support layer and functional layer in the measured pSOFC [32], while there is only one single Ni–YSZ anode layer in the measured mtSOFC [26]. Similarly, there are two cathode layers in the pSOFC and one cathode layer in the mtSOFC [26,32]. Since the data for the particle sizes were not reported in the mtSOFC experiment [26], our numerical simulation of the mtSOFC model uses the particle sizes (Table 2) that are intermediate to the values used for the pSOFC model [7,31] as a compromise. Similarly, intermediate values are used for the electrode porosities. In addition, the experiment on pSOFC found large contact resistance between the material layers [32]. As the inter-layer contact resistance was not examined for mtSOFC, the contact resistance was adjusted to fit the experimental mtSOFC I – V curves. The fit gives the total contact resistance of $0.04 \Omega \text{ cm}^2$, $0.05 \Omega \text{ cm}^2$ and $0.07 \Omega \text{ cm}^2$ for 800°C , 700°C and 600°C , respectively. These values are smaller than the corresponding pSOFC ones [32] and are quite reasonable as there are more material layers in the pSOFC than in the mtSOFC.

The theoretical and experimental I – V relations of mtSOFC at different working temperatures are compared in Fig. 2a. Good agreement between the theory and the experiment is found, demonstrating that the present thermal fluid electrochemistry model is capable of providing quality predictions. It also indicates that the material property parameters deduced mostly from independent experimental and theoretical results are of general applicability.

4.1.2. Effect of anode current collection on the electrochemical performance

The electrochemical performance of mtSOFC shown in Fig. 2a is much poorer than its pSOFC counterpart. One major contributing factor is the current collection mode. The contour of the current density distribution shown in Fig. 2b gives the hint for the poor performance. All current has to pass through the cross section determined by the anode layer thickness (and the perimeter of the mtSOFC tube) and the average length of the current passage equals roughly to the half of the tube (anode) length. If the current is collected by both sides of the anode current collector, the cross section area will be increased by a factor of two and the length for current passage will be reduced by half roughly, in comparison with the case of one-side current collection. The ohmic polarization is thus substantially reduced and an increased cell performance is expected. Indeed, significantly improved cell performance (Fig. 3a) is obtained by numerical simulation for the same mtSOFC with the current collection by both sides of the anode. Comparison of Figs. 3a and 2a show that the overall current output is increased by about 50%, demonstrating the critical importance of the current collection mode. As the current collection by both outer surfaces of the anode may be easily made experimentally, we focus on this current collection mode in the following numerical simulations. The cell with the default parameters and this current collection mode is referenced as the standard cell below.

4.1.3. Temperature profile

Fig. 4 shows the temperature profile of mtSOFC when operating at the fuel inlet temperature of 1073 K and the cell voltage of 0.7 V . The temperature varies from 1073 K to 1090.2 K for the cell with a tube length of 3 cm . As shown in Fig. 4, the two ends of the cell tube have a lower temperature than the middle of the cell tube and

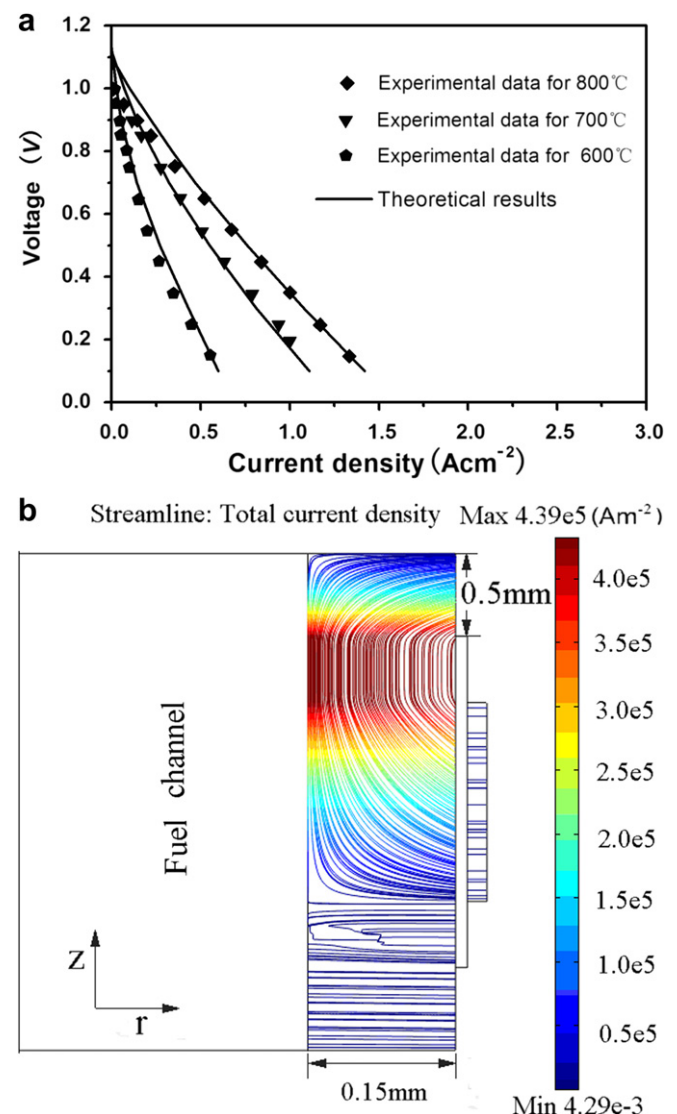


Fig. 2. Electrochemical performance of mtSOFC with the current collected by one side of the anode (a) comparison of the theoretical and experimental I – V results; (b) streamline of the electronic current density distribution in the electrodes for $T = 800^\circ\text{C}$ and $V_{cell} = 0.7\text{ V}$. The thickness direction (r -direction) is magnified for easy display.

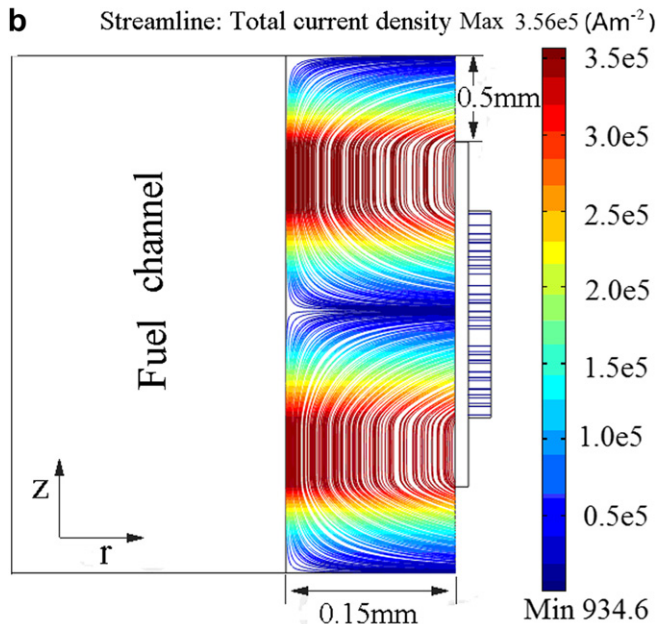
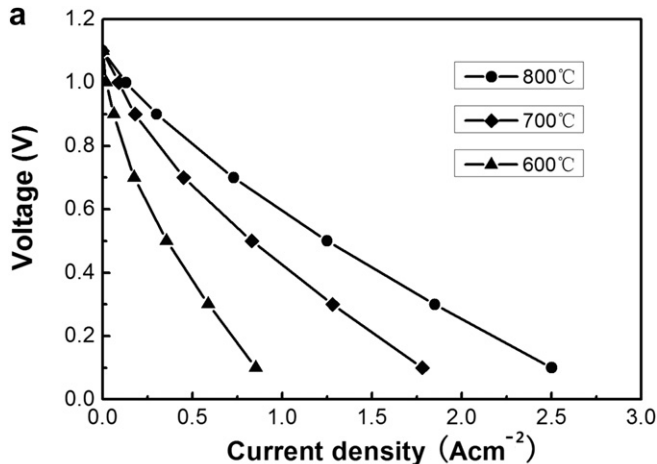


Fig. 3. mtSOFC with the current collected by both sides of the anode (a) I – V relations; (b) the electronic current density distribution for $T = 800$ °C and $V_{\text{cell}} = 0.7$ V.

the hotspot is located closer to the fuel exit end of the cell. The temperature variation of about 17 K along the cell tube of 3 cm is rather mild in comparison with that found for pSOFC [34]. The relatively uniform temperature distribution of mtSOFC indicates that mtSOFC may operate at a higher temperature for the increased power output than its pSOFC counterpart.

4.1.4. Stress distributions for $T_0 = 298$ K and $T_{\text{op}} = 1073$ K

The residual stress in the cell at room temperature depends on the cell fabrication process. For consistency, we consider the mtSOFC made by Yang et al. [26] and the relevant fabrication processes may be summarized as the following. The electrolyte layer was coated on to the anode surface using a vacuum assisted coating technique and then co-fired at 1723 K for 10 h to form a thin and dense layer. The cathode materials were coated on to the electrolyte by brush printing and sintered at 1423 K for 3 h. With these fabrication processes, the zero stress temperatures suggested for the anode, electrolyte and cathode are 1473 K, 1473 K and 1373 K, respectively [15,70]. We assume that the residual stresses are induced in the anode/electrolyte/cathode structures only due to the CTE mismatch between different layers. The thermal stress is introduced by the CTE mismatch and the temperature profile.

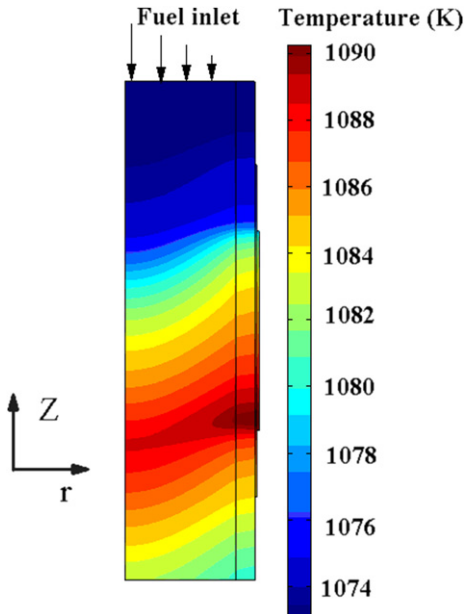


Fig. 4. Temperature profile of mtSOFC operated at 800 °C and 0.7 V.

Fig. 5a shows the residual stress distribution of the cell at room temperature. The blue, red and green lines stand for the first, second and third principal stresses, respectively. As shown in Fig. 5a, the stress in the anode is mostly tensile, while the stresses in the cathode and the electrolyte are mostly compressive. As the cell is manufactured at high temperature, it suffers a great residual stress at room temperature. The maximum residual compressive stress is 375 MPa for the electrolyte and 26 MPa for the cathode. The residual tensile stress for the anode is around 35 MPa.

Fig. 5b shows the stress distribution in the middle cross section of the cell at the operating temperature of 1073 K and the operating voltage of 0.7 V. The stress distribution is calculated with the temperature profile of the cell at the operating condition. Similar to the case for the room temperature, the stresses in the operating cell are mostly tensile for the anode and mostly compressive for the cathode and the electrolyte. The magnitudes of the thermal stresses in the operating cell are found to be smaller than that of the room temperature residual stresses. This is due to that the stress free temperatures are closer to the operating temperature than to the room temperature. The maximum compressive stress is about 123 MPa for the electrolyte and 7 MPa for the cathode. The maximum tensile stress of the anode is 14 MPa. Even though the thermal stress is smaller at the operating temperature than at room temperature, the mechanical strength of the electrode is also lower at the operating temperature. As to be seen below, the failure probability turns out to be higher at the operating temperature.

4.2. Effect of electrode composition on electrochemical performance

As seen in Section 2.1, the material compositions such as the volume fractions and the particle sizes of Ni/LSM/YSZ affect both the TPB lengths and electrical conductivities of the electrodes. Consequently, the material compositions affect both the activation and ohmic polarizations. Here we apply the mathematical model to examine the effects of the electrode compositions and their designs for improving the electrochemical performance.

4.2.1. Effect of electrode composition on the TPB length

As shown in Eq. (19), the anode (cathode) TPB length depends on the percolation probability of Ni (LSM) and YSZ, the average

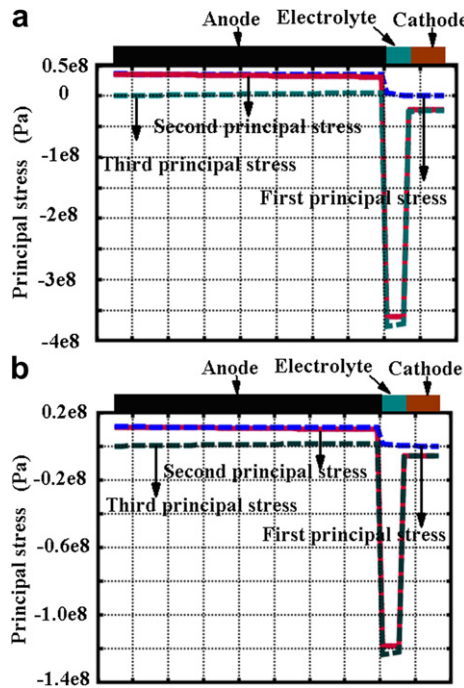


Fig. 5. Distributions of the first, second and third principal stresses of mtSOFC along the radial direction (a) $T = 298$ K, (b) $T_{op} = 1073$ K.

coordination number between Ni (LSM) and YSZ, and the number of Ni (LSM) particles per unit volume. The dependence of the percolated TPB length on the volume fraction and particle size of Ni (LSM) in the anode is shown in Fig. 6. The volume fraction of Ni (LSM) is varied from 0.3 to 0.7. The radius of the Ni (LSM) particle changes from 0.18×10^{-6} m (0.21×10^{-6} m) to 0.42×10^{-6} m (0.42×10^{-6} m), while the radius of the YSZ particle is kept at 0.3×10^{-6} m. The maximum lengths of the anode TPB for the Ni radii of 0.18×10^{-6} m, 0.33×10^{-6} m and 0.42×10^{-6} m are respectively 5.12×10^{12} m $^{-2}$, 3.12×10^{12} m $^{-2}$ and 2.26×10^{12} m $^{-2}$, corresponding to the Ni volume fractions of 0.39, 0.53 and 0.59, respectively. The anode TPB length normally increases with the decrease of the Ni radius due to the increased number of Ni particles per unit volume. However, the change of the Ni radius also affects the coordination numbers (Eq. (20)) and the percolation probabilities (Eq. (21)). The percolation regime shifts to smaller volume fraction of Ni when the Ni particle size decreases. Consequently, the Ni volume fraction corresponding to the maximal

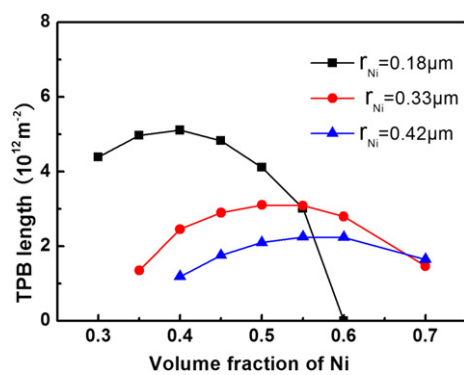


Fig. 6. Variation of the anode TPB length with the Ni volume fraction and the Ni radius. The radii of the YSZ particles are kept at 0.3×10^{-6} m.

TPB length decreases with the decreased Ni radius, as observed. The trend is the same for the cathode. The maximum lengths of the cathode TPB for the LSM radii of 0.21×10^{-6} m, 0.3×10^{-6} m and 0.42×10^{-6} m are respectively 4.47×10^{12} m $^{-2}$, 3.59×10^{12} m $^{-2}$ and 2.26×10^{12} m $^{-2}$, corresponding to the LSM volume fractions of 0.4, 0.5 and 0.59, respectively.

4.2.2. Effects of electrode composition on electrical conductivity

The effects of the Ni (LSM) volume fraction and particle size on the electronic and ionic conductivities of the anode (cathode) as determined by Eq. (14) are shown in Fig. 7 for the operating temperature of 1073 K. The electronic conductivity of the anode (cathode) increases with the increased Ni (LSM) volume fraction or the reduced Ni (LSM) particle size due to the increased relative abundance of the electronic conducting Ni (LSM) particles. Conversely, the ionic conductivity of the anode (cathode) decreases with the increased Ni (LSM) volume fraction or the reduced Ni (LSM) particle size for the same reason. An increased electronic conductivity is helpful for reducing the ohmic polarization of carrying the electronic current, while an increased ionic conductivity reduces the ohmic polarization of carrying the ionic current, allowing for the electrochemical reaction to take place in an increased distance from the electrolyte surface. The two competing factors, together with the consideration about the TPB length, should be properly balanced to obtain the desirable cell performance, as to be discussed below.

4.2.3. Effect of anode composition on electrochemical performance

Fig. 8a shows the average current densities for the cell operating voltages of 0.6, 0.7 and 0.85 V as functions of the Ni volume fraction. The Ni volume fractions for producing the maximum current densities for the three operating voltages are all about 0.65. That is, the optimal Ni volume fraction for the maximal current output is insensitive to the operating voltage. However, the current density changes more rapidly with the Ni content for the lower operating voltage than for the higher operating voltage. For example, the current densities for the cell voltage of 0.85 V, 0.7 V and 0.6 V are respectively 93%, 87% and 84% of their maximal when the Ni volume fraction is changed to 0.5 from its optimal value of 0.65. The stronger influence of the Ni volume fraction on the current output of the lower operating voltage is understandable as the current produced by the lower operating voltage is larger and is therefore more sensitive to the effect of the Ni content on the electrical conductivity and the TPB length.

Even though the anode electronic conductivity is much larger than the anode ionic conductivity for most of the Ni content examined (Fig. 7), the optimal electrode composition corresponds to a content of Ni higher than that of YSZ. This indicates that the anode electronic conductivity is more important than the anode ionic conductivity for the current output. The reason is that the electrochemical reaction happens at the TPBs near the electrode–electrolyte interface and the electronic current path is much longer than that of the ionic current path.

The combination effect of the volume fraction and particle size of Ni is shown in Fig. 8b. The maximal current output for the Ni radius of 0.18, 0.33 and 0.42×10^{-6} m is obtained with the Ni volume fraction of 0.55, 0.6 and 0.7, respectively. As shown in Fig. 8b, the maximal currents are not very different for different Ni radii. For example, the maximum current densities for the Ni radii of 0.42×10^{-6} m, 0.33×10^{-6} m and 0.18×10^{-6} m are $10,553 \text{ A m}^{-2}$, $10,846 \text{ A m}^{-2}$ and $10,992 \text{ A m}^{-2}$, respectively. However, the current output decreases more slowly for smaller Ni particles than for larger Ni particles when the Ni volume fractions deviate away from their optimal values. The current density for the Ni radius of 0.18×10^{-6} m is about 88% of its maximum when the Ni

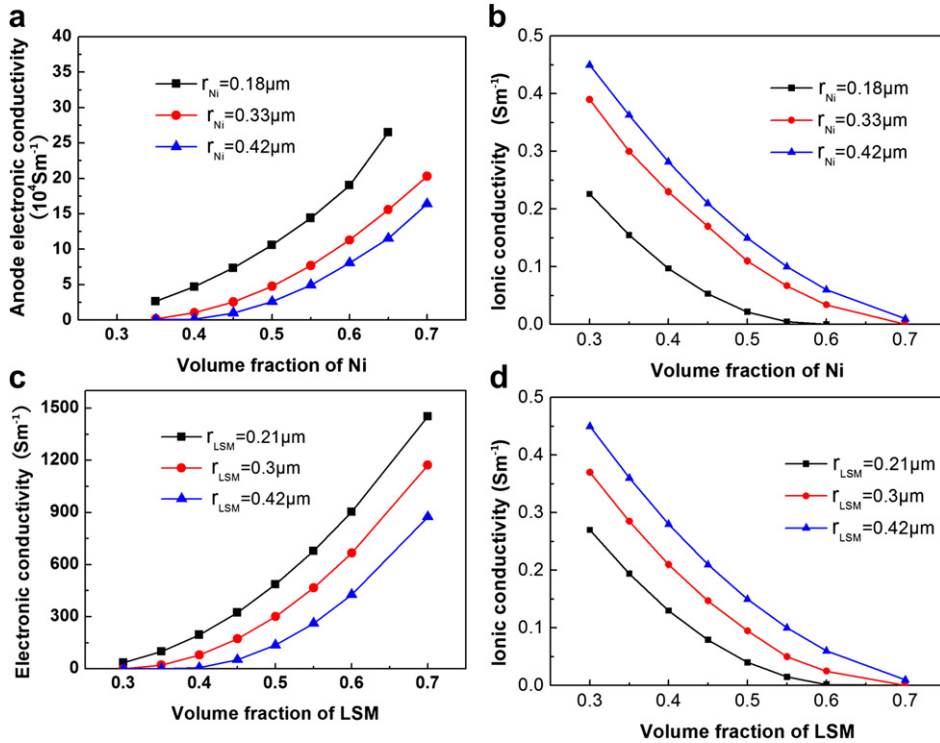


Fig. 7. Influence of the material composition on the electrode electrical conductivity at $T = 1073$ K. (a) Electronic conductivity of the anode vs. the Ni volume fraction and particle size; (b) ionic conductivity of the anode vs. the Ni volume fraction and particle size; (c) electronic conductivity of the cathode vs. the LSM volume fraction and particle size; (d) ionic conductivity of the cathode vs. the LSM volume fraction and particle size.

volume fraction is 0.4, or a deviation of about 12% from the optimal Ni volume fraction of 0.55. For a similar amount of deviation, the current outputs for the Ni radii of 0.33×10^{-6} m and 0.42×10^{-6} m are only about 62% and 16% of their maxima, respectively.

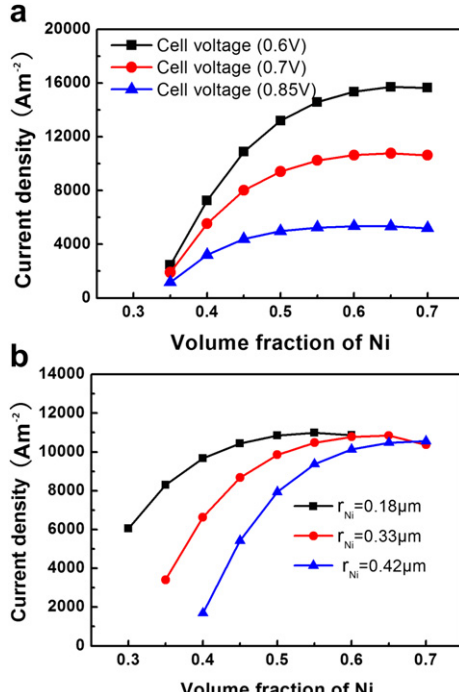


Fig. 8. Effect of the anode composition on the cell output (a) current density vs. the Ni volume fraction and the operating voltage; (b) current density vs. the Ni volume fraction and particle size.

Therefore, using small Ni particle sizes allows for a large adjustable range of the Ni content while maintaining the desirable current production.

4.2.4. Effect of cathode composition on electrochemical performance

The dependence of the cell current output on the operating voltage and the LSM volume fraction is shown in Fig. 9a. The volume fraction of LSM for producing the maximum output is about 0.4. Unlike the case for the anode, the cathode should have more YSZ than LSM to be optimal. That is, the cathode ionic conductivity is often more important than the cathode electronic conductivity for the current output. This is characteristically different from that of the anode. The phenomena is attributed to that the electrochemical reaction in the cathode is much slower than that in the anode. High cathode ionic conductivity is important for increasing the reaction region and reducing the activation polarization.

Above the optimal LSM volume fraction of 0.4, the current density increases with the decrease of the LSM volume fraction. Below the optimal LSM content, the current density initially decreases slowly with the decrease of the LSM volume fraction, but drops rapidly when the LSM volume fraction is approaching 0.3. This is because that the percolation probability of the LSM particle network is low for the LSM volume fraction below 0.35, resulting in an unacceptably low electronic conductivity of the cathode (Fig. 7c, $r_{\text{LSM}} = 0.3 \mu\text{m}$).

Fig. 9b shows the combined effect of the volume fraction and particle size of LSM on the current output. The maximal current outputs for the LSM radii of 0.21 , 0.3 and 0.42×10^{-6} m are obtained with the LSM volume fraction of 0.3, 0.4 and 0.5, respectively. Compared to the case for the anode Ni composition, the dependence of the maximal current density on the LSM particle size is relatively large due to the relatively strong effect of the TPB on the cathode electrochemical reaction. The maximum current density

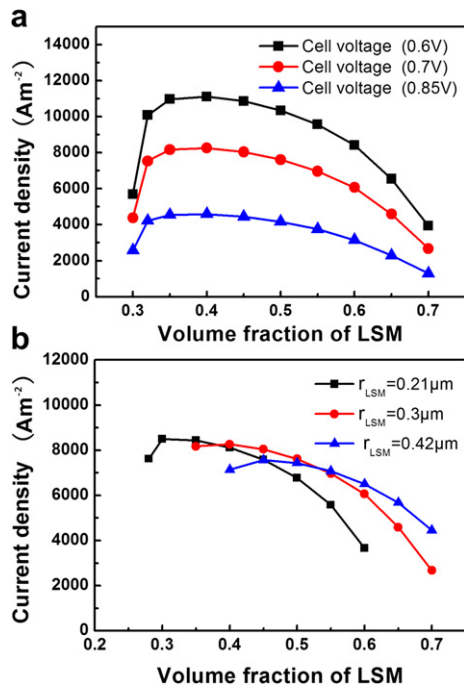


Fig. 9. Effect of the cathode composition on the cell output (a) current density vs. the LSM volume fraction and the operating voltage; (b) current density vs. the LSM volume fraction and particle size.

increases from 7565 A m^{-2} – 8498 A m^{-2} , or an increase of 12%, when the LSM radius is decreased from $0.42 \times 10^{-6} \text{ m}$ to $0.21 \times 10^{-6} \text{ m}$. It is desirable to use small LSM particle to improve the cell output.

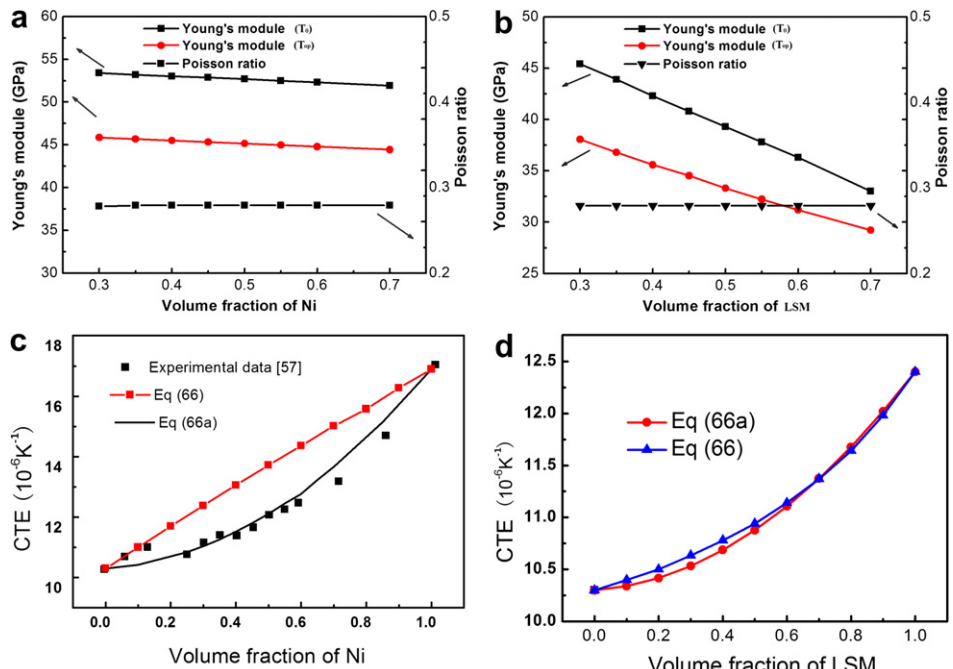


Fig. 10. Dependences of the thermal mechanical properties on the electrode compositions (a) Young's module and Poisson ratio of the anode vs. the Ni volume fraction; (b) Young's module and Poisson ratio of the cathode vs. the LSM volume fraction; (c) anode CTE as a function of the Ni volume fraction (the experimental data are taken from Ref. [59]); (d) cathode CTE vs. the LSM volume fraction.

4.3. Effect of electrode composition on thermal mechanical performance

4.3.1. Effect of electrode composition on thermal mechanical properties

The compositions affect the thermal mechanical properties of the electrodes according to the theory described in Section 2.3. The Poisson ratios of pure Ni, YSZ and LSM as well as the Young's module of LSM at the mtsOFC operating temperature are assumed here to be the same as the ones at room temperature. Fig. 10a (Fig. 10b) shows the variations of the anode (cathode) Young's module and Poisson ratio with the volume fraction of Ni (LSM). As the Poisson ratios of Ni (LSM) and YSZ are very similar, the Poisson ratio of the Ni–YSZ composite anode (LSM–YSZ composite cathode) remains almost constant with the variation of the Ni (LSM) volume fraction. In the other hand, the Young's module shows a larger variation with the LSM volume fraction for the cathode than with the Ni volume fraction for the anode as the difference in the Young's module is larger between YSZ and LSM than between YSZ and Ni.

Fig. 10c shows the anode CTE as a function of the Ni volume fraction. As the CTEs of Ni and YSZ are very different, applying Eq. (66) to the Ni–YSZ composite anode is found to produce sizable deviations from the available experimental data [56]. Numerical tests show that the mechanical failure probabilities of the electrodes are sensitive to the anode CTE. Therefore, it is necessary to improve the numerical quality of the anode CTE for the interested Ni content ($\psi_{\text{Ni}} \in [0.3, 0.7]$). For that purpose, the CTE of the Ni–YSZ composite anode for the structural mechanics model is calculated by the following empirical fitting expression:

$$\text{CTE}_{\text{anode}} = \text{CTE}_{\text{YSZ}} + (\text{CTE}_{\text{Ni}} - \text{CTE}_{\text{YSZ}})\psi_{\text{Ni}}(0.1 + 0.9\psi_{\text{Ni}}) \quad (66a)$$

As seen in Fig. 10c, our fitting expression of Eq. (66a) agrees reasonably well with the experimental result.

The cathode CTE as a function of the LSM volume fraction as determined by Eq. (66) is shown in Fig. 10d. As the CTEs of LSM and YSZ are only moderately different, Eq. (66) should provide a good estimate of the CTE of the LSM–YSZ composite cathode. In fact, as shown in Fig. 10d, the results by Eq. (66) for any LSM volume fractions are in good agreement with the results by the analog of Eq. (66a) for the cathode, $CTE_{\text{cathode}} = CTE_{\text{YSZ}} + (CTE_{\text{LSM}} - CTE_{\text{YSZ}}) \psi_{\text{LSM}}(0.1 + 0.9\psi_{\text{LSM}})$. This comparison may be seen as indirect evidence that the cathode CTE is determined with good accuracy. Moreover, Fig. 10c and d seems to imply that Eq. (66) is only valid for the composite consisting of two components with similar CTEs, while Eq. (66a) is valid even when the CTEs of the two components are substantially different. However, as numerical results show that the mechanical failure probabilities of the electrodes are not sensitive to the cathode CTE and to conform to the mainstream literature, Eq. (66) is used to determine the CTE of the composite cathode in the following study.

4.3.2. Effect of anode composition on mechanical failure

As described in Section 2.4, the tensile failure of the ceramic components of the cell is analyzed using the Weibull statistical method, while the mechanical failure occurs when the maximum compressive stress exceeds the compress strength of the material. The sizes of the Ni and LSM particles do not affect the mechanical properties in the model used here. As described above, the particle sizes do affect the electrochemical performance. However, their effect on the temperature profile is rather moderate due to the small dimension of the mtSOFC. Therefore, the analysis of the failure probability is only slightly affected by the particle sizes. The following analysis uses a Ni radius of 0.18 μm and a LSM radius of 0.3 μm as the representing case.

Fig. 11a shows the tensile failure probabilities of the electrodes at room temperature as functions of the Ni content in the anode. The failure probability of the anode is only 3.8×10^{-11} for the Ni volume fraction of 0.3, but increases to 0.0019 when the Ni volume

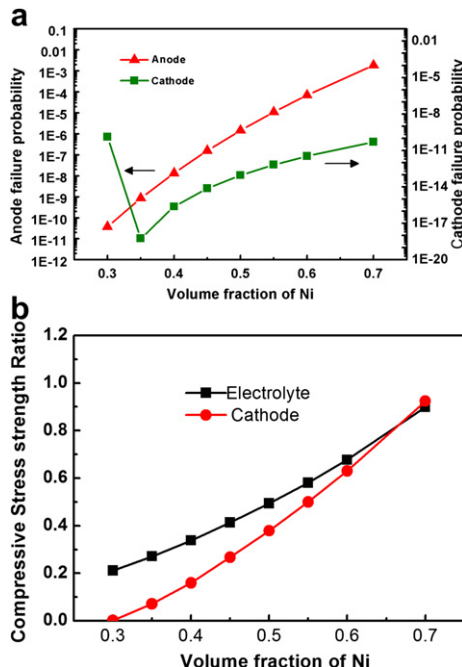


Fig. 11. Dependence of the mechanical failure at room temperature on the anode composition (a) failure probabilities of the electrodes vs. the Ni volume fraction; (b) ratios of the maximum compressive stresses of the electrolyte and the cathode to their compressive strengths as functions of the Ni volume fraction.

fraction is increased to 0.7. It has been proposed that the failure probability should be under 10^{-5} to ensure mechanical stability [71]. Based on this criterion, the Ni volume fraction should be below 0.5. The failure probability of the cathode is smaller than 10^{-9} for all interested Ni content and the Ni content is inconsequential to the mechanical stability of the cathode.

Fig. 11b shows the compressive stress strength ratios of the electrolyte and the cathode, the ratios of the maximum compressive stresses of the electrolyte and the cathode to their compressive strengths, at room temperature. For the range of the Ni volume fraction examined, the ratios are smaller than 1 and the mechanical fracture is not expected. Therefore, all interested Ni volume fraction meets the requirement for the mechanical stability of the electrolyte and cathode.

Fig. 12a shows the failure probabilities of the electrodes at the operating temperature as functions of the Ni volume fraction. The anode failure probability increases from 2.93×10^{-7} to 0.003 when the Ni volume fraction increases from 0.3 to 0.7, while the cathode failure probability remains below 10^{-9} . The numerical result on the failure probability clearly shows that increasing the Ni content may easily bring about mechanical flaw in the anode, agreeing well with experimental observation [27]. Considering the criterion of the failure probability of 10^{-5} for the mechanical safety, the Ni volume fraction should not exceed 0.42.

The compressive stress strength ratios of the electrolyte and the cathode at the operating temperature are shown in Fig. 12b. Unlike the case for the room temperature, the mechanical failure is expected for the electrolyte when the Ni volume fraction exceeds 0.65. As the mechanical stability of the anode requires a lower Ni volume fraction, the Ni content is determined by the anode stability.

4.3.3. Effect of cathode composition on mechanical failure

The effect of the LSM content on the failure probabilities of the electrodes and the compressive stress strength ratios of the

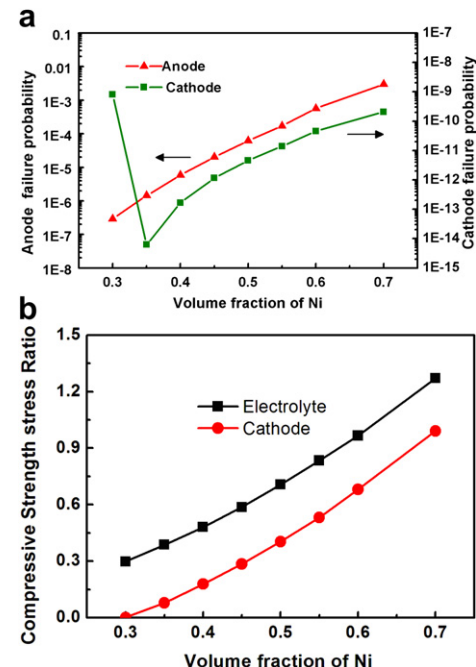


Fig. 12. Dependence of the mechanical failure at the operating temperature on the anode composition (a) failure probabilities of the electrodes vs. the Ni volume fraction; (b) compressive stress strength ratios of the electrolyte and the cathode vs. the Ni volume fraction.

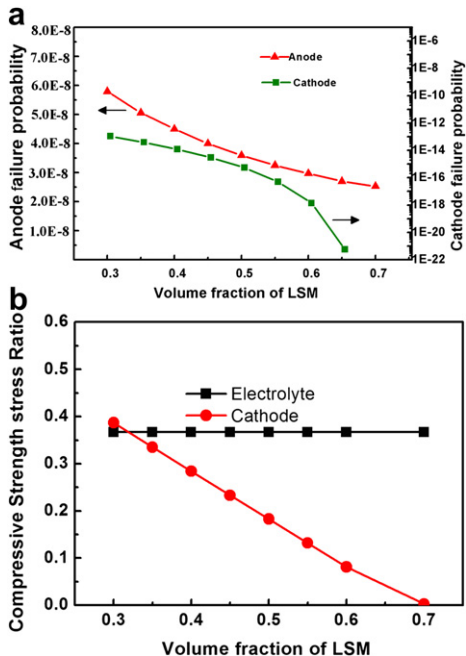


Fig. 13. Dependence of the mechanical failure at room temperature on the cathode composition (a) failure probabilities of the electrodes vs. the LSM volume fraction; (b) compressive stress strength ratios of the electrolyte and the cathode vs. the LSM volume fraction.

electrolyte and the cathode at room temperature is shown in Fig. 13. The failure probabilities of the electrodes decrease with the increase of the LSM content due to that the increased CTE of the cathode matches better with that of the anode, reducing the tensile stresses of both the electrodes as well as the compressive stress of the cathode. The electrode failure probability is smaller than 6×10^{-8} for all interested LSM volume fraction and is well under the failure probability of 10^{-5} for mechanical stability. The compressive stress strength ratios of the electrolyte and the cathode are less than 0.4 for all interested LSM volume fraction and are safe mechanically.

The effect of the LSM content on the failure probabilities of the electrodes and the compressive stress strength ratios of the electrolyte and the cathode at the operating temperature is shown in Fig. 14. The failure probability of the anode changes slowly with the LSM content. It decreases from 1.26×10^{-5} to 9.0×10^{-6} when the LSM volume fraction increases from 0.3 to 0.7. These failure probabilities are at the borderline of 10^{-5} for mechanical security and should be acceptable in practice. The compressive stress strength ratios of the electrolyte and the cathode are less than 0.6 for all interested LSM volume fraction and are safe mechanically.

As seen from the above discussion, the LSM content is inconsequential from the mechanical stability point of view. The LSM content should be determined by the optimal electrochemical performance of the cell.

4.4. Primitive comparison of the current outputs of mtSOFC and pSOFC

mtSOFCs have long been recognized for their high performance on the thermal shock resistance, fast startup and thermal cycling. However, the current density output of mtSOFC is widely shown to be comparable with or moderately superior over its tSOFC counterpart, but is substantially inferior to the pSOFC [2,26]. Nevertheless, as discussed above, the current output of mtSOFC may be significantly increased by changing the current collection from one

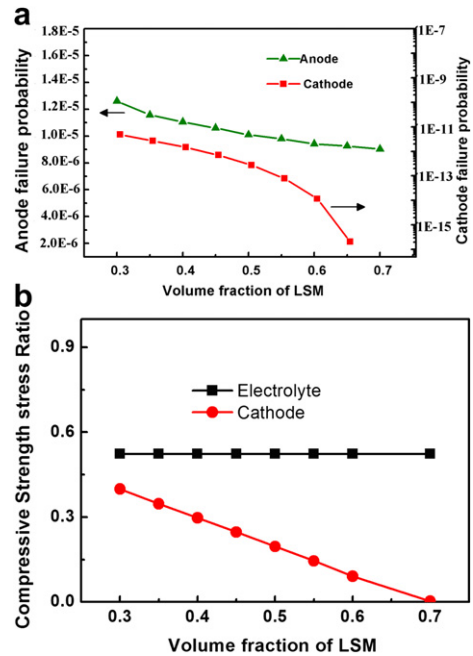


Fig. 14. Dependence of the mechanical failure at the operating temperature on the cathode composition (a) failure probabilities of the electrodes vs. the LSM volume fraction; (b) compressive stress strength ratios of the electrolyte and the cathode vs. the LSM volume fraction.

side of the anode, which is the main method currently in use [2,26], to both sides of the anode. In fact, the current production shown in Fig. 3a is not very far away from the state-of-the-art performance of pSOFC [32]. It would be interesting to make a comparison of the current outputs of mtSOFC and pSOFC on a reasonably equal basis. However, due to the involvement of a large number of different design parameters, a quality comparison of the mtSOFC and pSOFC performances requires a specifically devoted effort and only a primitive comparison is attempted here.

In Ref. [32], the electrochemical performance of pSOFC is systematically improved over that of a standard cell by optimizing the electrolyte thickness, cathode interlayer thickness, anode support layer thickness and anode support porosity, while the performance of their standard cell is already very close to the best reported by other pSOFC groups using the same set of materials. Therefore, it is reasonable to use the standard cell performance of Ref. [32] as the benchmark for comparison here. The standard cell of mtSOFC defined above is modified in order to compare with the standard cell of pSOFC in Ref. [32] on an equal basis. The changes made to the standard cell of mtSOFC are: 8 μm for the electrolyte thickness, 26% for the cathode porosity, 23% for the anode porosity. These data are the corresponding parameters for the standard pSOFC cell and the modified standard mtSOFC cell may then mimic the standard pSOFC cell better. The I – V curves of the mtSOFC and pSOFC cells are compared in Fig. 15.

As shown in Fig. 15, the power densities of the standard mtSOFC and pSOFC cells are quite similar for the operating temperature of 700 $^{\circ}\text{C}$. The maximal power density of the pSOFC cell is higher than that of the mtSOFC cell for $T = 800$ $^{\circ}\text{C}$, but is lower than that of mtSOFC for $T = 600$ $^{\circ}\text{C}$. For practical applications, SOFC has to work at a relatively high voltage (typically 70–80% of the open voltage) in order to have the desirable energy efficiency. In such cases, the performances of the mtSOFC and pSOFC cells are essentially the same, as may be easily seen in Fig. 15. Therefore, it is concluded that the output current density of mtSOFC with proper current collection is similar to instead of much smaller than that of pSOFC.

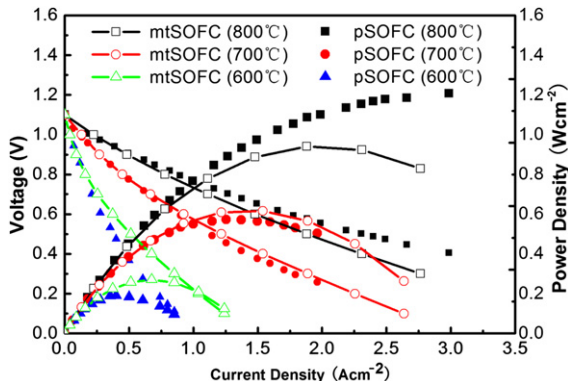


Fig. 15. Comparison of the electrochemical performances of the standard mtSOFC and pSOFC cells.

5. Summary

We have described in detail a thermal fluid electrochemistry model for the study of the electrochemical performance of SOFC. The model couples the intricate interdependency among the ionic conduction, electronic conduction, gas transport, electrochemical reaction, thermal conduction and heat exchange with the environment, and takes into account the contact resistance between the cell components and the dependence of the effective electrode properties on the microstructure parameters of the porous electrodes. The validity of the mathematical model is demonstrated by the excellent agreement between the theoretical and experimental I – V curves of mtSOFC operated at different temperatures. The numerical model is used to study the effects of the particle sizes and volume fractions of Ni and LSM as well as the anode current collection mode on the electrode properties and current production of mtSOFC with the typical Ni–YSZ anode, YSZ electrolyte and LSM–YSZ cathode. The critical importance of anode current collection is revealed and the current output of mtSOFC may be drastically increased by collecting current from both sides instead of one side of the anode. This finding should be helpful for guiding the experimentalists to design improved mtSOFCs.

We have also described a thermal mechanical model for the analysis of the mechanical behavior of SOFC, with the thermal mechanical properties determined by the available theory and experiment and linked to the compositions of the materials. Based on given temperature profiles, e.g., the results by the simulations of the thermal fluid electrochemistry model, the mechanical model can calculate the thermal stress distributions of the mtSOFC components, followed with the mechanical failure analysis using the Weibull model. Numerical results show that the stresses are tensile for the Ni–YSZ anode and mostly compressive for the YSZ electrolyte and LSM–YSZ cathode. The anode, electrolyte and cathode suffer higher stresses at room temperature than at the cell operating temperature. However, the mechanical failure probability is higher at the cell operating temperature than at room temperature as the mechanical strengths of the materials decrease with the increased temperature.

Optimizations of the electrode microstructure and composition for both the electrochemical and mechanical performances of mtSOFC are considered. Increasing the Ni content or reducing the Ni particle size is generally helpful for improving the electrochemical performance. However, the tensile stress and the accompanying failure probability of the anode and the compressive stresses of the electrolyte and cathode all increase with the increased Ni content. Overall, a Ni volume fraction of about 0.4 and a Ni particle size smaller than the YSZ particle size are

recommended to obtain both high electrochemical performance and mechanical stability. Regarding the cathode material, the best electrochemical performance of the cell is often obtained with a LSM volume fraction of 30–50%. The optimal LSM content decreases, while the overall electrochemical performance increases, with the reduced LSM particle size. Increasing the LSM content reduces the compressive stress of the cathode, but its effects on the anode and electrolyte stresses are very limited. Overall, the LSM content is inconsequential on the mechanical stability and should be optimized based on achieving high electrochemical performance.

A primitive comparison of the I – V curves of mtSOFC and pSOFC is made. It is concluded that the current outputs of pSOFC and mtSOFC are in fact comparable if a proper current collection method is used in mtSOFC. Therefore, mtSOFC is a promising technology with both the benefits of pSOFC for high current density and tSOFC for thermal cycling endurance.

Acknowledgments

The financial support of the National Basic Research Program of China (973 Program Grant No. 2012CB215405), the National Natural Science Foundation of China (Grant No. 11074233) and the Specialized Research Fund for the Doctoral Program of Higher Education (Grant No. 20113402110038) are gratefully acknowledged.

Nomenclature

a_i^1 , a_i^2 , a_i^3	coefficient of the specific heat of material species i , ($\text{J kg}^{-1} \text{K}^{-1}$)
b_i^1 , b_i^2 , b_i^3	coefficient of the thermal conductivity of material species i , ($\text{W m}^{-1} \text{K}^{-1}$)
B_0	permeability coefficient, (m^2)
C_i	molar concentration of species i , (mol m^{-3})
C_p	effective specific heat of the fluid, ($\text{J mol}^{-1} \text{K}^{-1}$)
c_{ref}	Sutherland's constant.
D	elasticity matrix,
D_i	diffusion coefficient of species i , ($\text{m}^2 \text{s}^{-1}$)
$D_{ij}(D_{ij}^{\text{eff}})$	(effective) binary diffusion coefficient, ($\text{m}^2 \text{s}^{-1}$)
D_{iK}^{eff}	effective Knudsen diffusion coefficient of species i , ($\text{m}^2 \text{s}^{-1}$)
d	hydraulic diameter, (m)
$E(E_{\text{eff}})$	(effective) Young's modulus, (GPa)
E_0	Nernst potential, (V)
$E_{\text{H}_2}(E_{\text{O}_2})$	activation energy for the anode (cathode), (J mol^{-1})
$G(G_{\text{eff}})$	(effective) Shear modulus, (GPa)
ΔG^0	free energy change, (J mol^{-1})
h	heat transfer coefficient, ($\text{W m}^{-1} \text{K}^{-1}$)
$i_{\text{el}}(\vec{i}_{\text{io}})$	charge transfer rate, (A m^{-3})
j_0	vector of electronic (ionic) current density, (A m^{-2})
$j_{0,\text{ref}}(j_{0,\text{ref}}^c)$	exchange transfer current per unit three phase boundary (TPB) length, (A m^{-1})
j_{TPB}	anode (cathode) exchange transfer current density at the reference temperature, (A m^{-1})
K_i	specific transfer current density, (A m^{-1})
K_{eff}	bulk modulus, (GPa)
k_{eff}	effective thermal conductivity, ($\text{W m}^{-1} \text{K}^{-1}$)
$k_f(k_s)$	effective thermal conductivity of the fluid (solid), ($\text{W m}^{-1} \text{K}^{-1}$)
M	molecular mass, (kg mol^{-1})
N_i	molar flux of species i , ($\text{mol m}^{-2} \text{s}^{-1}$)
N_u	Nusselt number
n_k^V	number of k -particles per unit volume in a composite electrode
$P_{\text{ed}}(P_{\text{el}})$	Percolation probability of electrode (electrolyte) particles

P_f	failure probability of the cell component
$p_{H_2}(p_{H_2O}, p_{O_2})$	partial pressure of H_2 (H_2O, O_2), (Pa)
Q	heat source, ($W\ m^{-3}$)
Q_{act} (Q_{entr}, Q_{entr})	activation (entropy, ohmic) heat source, ($W\ m^{-3}$)
R	universal gas constant, ($J\ mol^{-1}\ K^{-1}$)
R_i	reaction rate of species i at TPB, ($mol^{-1}\ m^{-3}\ s^{-1}$)
R_{ASR}	contact resistance, ($\Omega\ cm^2$)
r_g	pore radius, (m)
r_k	radius of k particle, (m)
T	temperature, (K)
T_0	room temperature
T_{ext}	external temperature of air, (K)
T_f	stress free temperature, (K)
T_{fw}	temperature of the furnace wall, (K)
T_{op}	cell operating temperature, (K)
T_{ref}	reference temperature, (K)
\bar{u}	vector of convection velocity, ($m\ s^{-1}$)
u_0	fuel flow rate, ($m\ s^{-1}$)
V_{cell}	operating cell voltage, (V)
\bar{Z}	average coordination number of all solid particles
$Z_{l,k}$	average number of l -particles in contact with a k -particle

Greek letters

α	coefficient of thermal expansion, (K^{-1})
α_{com}	coefficient of thermal expansion of composite material, (K^{-1})
σ	stress tensor, (MPa)
σ_0	initial stress or the residual stress, (MPa)
σ_{el}^{eff} (σ_{io}^{eff})	effective electronic (ionic) conductivity, ($S\ m^{-1}$)
σ_k^0	intrinsic conductivity of material k , ($S\ m^{-1}$)
σ_{ten}	tensile stress, (MPa)
ε_{rad}	surface emissivity
ζ	strain
ζ_{el}	elastic strain
ζ_{th}	thermal strain
ζ_0	initial strain
ϕ_{el} (ϕ_{io})	local electronic (ionic) potential, (V)
ψ_k (ψ_l)	volume fraction of k -phase (l -phase)
ψ_k^t	percolated volume fraction threshold of the k material
η_{act}	activation polarization, (V)
η_{act}^a (η_{act}^c)	anode (cathode) activation polarization, (V)
η_{ohm}^a (η_{ohm}^c)	electronic ohmic overpotential of anode (cathode), (V)
$\eta_{ohm}^{a,i}$ ($\eta_{ohm}^{c,i}$)	ionic ohmic overpotential of anode (cathode, electrolyte), (V)
η_{ASR}	contact ohmic overpotential, (V)
η_{con}^a (η_{con}^c)	concentration balance potential of anode (cathode), (V)
ρ	density, ($kg\ m^{-3}$)
θ	angle of particle contact
$\lambda_{TPB,eff}$	effective volume specific TPB length, (m^{-2})
μ	effective viscosity coefficient of fluid mixture, ($Pa\ s$)
μ_i (μ_j)	viscosity coefficient of species i (j), ($Pa\ s$)
μ_{ref}	viscosity at the reference temperature, ($Pa\ s$)
τ	tortuosity factor
$v(v_{eff})$	(effective) Poisson's ratio
ν	diffusion volume, ($m^3\ mol^{-1}$)

References

- [1] S.C. Singhal, K. Kendall, High Temperature Solid Oxide Fuel Cells: Fundamentals, Design, and Applications, Elsevier Science, 2003.
- [2] V. Lawlor, S. Griesser, G. Buchinger, A. Olabi, S. Cordiner, D. Meissner, Journal of Power Sources 193 (2009) 387–399.
- [3] N.Q. Minh, Journal of the American Ceramic Society 76 (1993) 563–588.
- [4] J. Deseure, Y. Bultel, L. Dessemond, E. Siebert, Electrochimica Acta 50 (2005) 2037–2046.
- [5] H. Zhu, R.J. Kee, Journal of Power Sources 117 (2003) 61–74.
- [6] J. Fleig, Annual Review of Materials Research 33 (2003) 361–382.
- [7] D. Chen, W. Bi, W. Kong, Z. Lin, Journal of Power Sources 195 (2010) 6598–6610.
- [8] S. Kakaç, A. Pramuanjaroenkij, X.Y. Zhou, International Journal of Hydrogen Energy 32 (2007) 761–786.
- [9] D. Bhattacharya, R. Rengaswamy, Industrial & Engineering Chemistry Research 48 (2009) 6068–6086.
- [10] S. DeCaluwe, H. Zhu, R.J. Kee, G.S. Jackson, Journal of the Electrochemical Society 155 (2008) B538.
- [11] D.H. Jeon, J.H. Nam, C.-J. Kim, Journal of the Electrochemical Society 153 (2006) A406–A417.
- [12] J. Li, Z. Lin, International Journal of Hydrogen Energy 37 (2012) 12925–12940.
- [13] A. Nakajo, Z. Wuillemin, J. Van Herle, D. Favrat, Journal of Power Sources 193 (2009) 203–215.
- [14] M.F. Serincan, U. Pasaogullari, N.M. Sammes, Journal of Power Sources 195 (2010) 4905–4914.
- [15] A. Atkinson, B. Sun, Materials Science and Technology 23 (2007) 1135–1143.
- [16] M. Peksen, R. Peters, L. Blum, D. Stolten, International Journal of Hydrogen Energy 36 (2011) 6851–6861.
- [17] H. Yakabe, Y. Baba, T. Sakurai, Y. Yoshitaka, Journal of Power Sources 135 (2004) 9–16.
- [18] H. Yakabe, M. Hishinuma, M. Uratani, Y. Matsuzaki, I. Yasuda, Journal of Power Sources 86 (2000) 423–431.
- [19] H. Yakabe, Y. Baba, I. Yasuda, in: Solid Oxide Fuel Cells VII (SoFC VII) (2001), pp. 303–310.
- [20] A. Selimovic, M. Kemm, T. Torisson, M. Assadi, Journal of Power Sources 145 (2005) 463–469.
- [21] K.S. Weil, B.J. Koeppl, International Journal of Hydrogen Energy 33 (2008) 3976–3990.
- [22] A. Nakajo, C. Stiller, G. Härkegård, O. Bolland, Journal of Power Sources 158 (2006) 287–294.
- [23] A. Nakajo, Z. Wuillemin, J. Van Herle, D. Favrat, Journal of Power Sources 193 (2009) 216–226.
- [24] M. Peksen, R. Peters, L. Blum, D. Stolten, International Journal of Hydrogen Energy 36 (2011) 4400–4408.
- [25] C.K. Lin, L.H. Huang, L.K. Chiang, Y.P. Chyou, Journal of Power Sources 192 (2009) 515–524.
- [26] C. Yang, W. Li, S. Zhang, L. Bi, R. Peng, C. Chen, W. Liu, Journal of Power Sources 187 (2009) 90–92.
- [27] M. Marinsek, K. Zupan, J. Macek, Journal of Power Sources 86 (2000) 383–389.
- [28] D. Cui, M. Cheng, AIChE Journal 55 (2009) 771–782.
- [29] U. Doraswami, N. Droushiotis, G. Kelsall, Electrochimica Acta 55 (2010) 3766–3778.
- [30] S. Liu, W. Kong, Z. Lin, Energies 2 (2009) 427–444.
- [31] W. Kong, J. Li, S. Liu, Z. Lin, Journal of Power Sources 204 (2012) 106–115.
- [32] F. Zhao, A.V. Virkar, Journal of Power Sources 141 (2005) 79–95.
- [33] D. Chen, Z. Lin, H. Zhu, R.J. Kee, Journal of Power Sources 191 (2009) 240–252.
- [34] M.A. Khaleel, Z. Lin, P. Singh, W. Surdoval, D. Collin, Journal of Power Sources 130 (2004) 136–148.
- [35] R. O'Hare, S.W. Cha, W. Colella, F.B. Prinz, Fuel cell fundamentals, John Wiley & Sons, USA, 2006.
- [36] H. Zhu, R.J. Kee, Journal of the Electrochemical Society 155 (2008) B715–B729.
- [37] J. Wu, D. McLachlan, Physical Review B 56 (1997) 1236.
- [38] P. Costamagna, P. Costa, V. Antonucci, Electrochimica Acta 43 (1998) 375–394.
- [39] D. Bouvard, F. Lange, Acta Metallurgica et Materialia 39 (1991) 3083–3090.
- [40] Y. Shi, N. Cai, C. Li, Journal of Power Sources 164 (2007) 639–648.
- [41] B. Todd, J.B. Young, Journal of Power Sources 110 (2002) 186–200.
- [42] K. Tseronis, I.K. Kookos, C. Theodoropoulos, Chemical Engineering Science 63 (2008) 5626–5638.
- [43] S. Liu, W. Kong, Z. Lin, Journal of Power Sources 194 (2009) 854–863.
- [44] P. Mandin, C. Bernay, S. Tran-Dac, A. Broto, D. Abes, M. Cassir, Fuel Cells 6 (2006) 71–78.
- [45] E.N. Fuller, P.D. Schettler, J.C. Giddings, Industrial & Engineering Chemistry 58 (1966) 19.
- [46] J.H. Nam, D.H. Jeon, Electrochimica Acta 51 (2006) 3446–3460.
- [47] A.B. COMSOL, COMSOL MULTIPHYSICS® Version 3.5 User's Guide (2007).
- [48] F.P. Incropera, D.P. Dewitt, Fundamentals of Heat and Mass Transfer, Wiley, Asia, 2007, pp. 572–575.
- [49] L. Petrucci, S. Cocchi, F. Fineschi, Journal of Power Sources 118 (2003) 96–107.
- [50] S. Campanari, P. Iora, Journal of Power Sources 132 (2004) 113–126.
- [51] Y. Kamotani, L. Wang, S. Hatta, A. Wang, S. Yoda, International Journal of Heat and Mass Transfer 46 (2003) 3211–3220.
- [52] D. Cui, M. Cheng, Journal of Power Sources 192 (2009) 400–407.
- [53] J. Laurencin, G. Delette, F. Lefebvre-Joud, M. Dupeux, Journal of the European Ceramic Society 28 (2008) 1857–1869.
- [54] Z. Hashin, S. Shtrikman, Journal of the Mechanics and Physics of Solids 11 (1963) 127–140.
- [55] N. Ramakrishnan, V.S. Arunachalam, Journal of Materials Science 25 (1990) 3930–3937.
- [56] D. Hull, T. Clyne, An Introduction to Composite Materials, Cambridge Univ Pr, 1996.
- [57] R. Vassen, N. Czech, W. Mallener, W. Stamm, D. Stöver, Surface and Coatings Technology 141 (2001) 135–140.
- [58] D.J. Green, An Introduction to the Mechanical Properties of Ceramics, Cambridge Univ Pr, 1998.

- [59] M. Mori, T. Yamamoto, H. Itoh, H. Inaba, H. Tagawa, *Journal of the Electrochemical Society* 145 (1998) 1374.
- [60] Y. Ji, J. Kilner, M. Carolan, *Solid State Ionics* 176 (2005) 937–943.
- [61] M. Radovic, E. Lara-Curzio, *Journal of the American Ceramic Society* 87 (2004) 2242–2246.
- [62] R. Farraro, R. McLellan, *Metallurgical and Materials Transactions A* 8 (1977) 1563–1565.
- [63] R.A. Cutler, D.L. Meixner, *Solid State Ionics* 159 (2003) 9–19.
- [64] R.N. Basu, F. Tietz, O. Teller, E. Wessel, H.P. Buchkremer, D. St ver, *Journal of Solid State Electrochemistry* 7 (2003) 416–420.
- [65] W. Weibull, in: *Proceedings of the Royal Swedish Institute of Engineering Research*, vol. 151, 1939, pp. 1–45.
- [66] C. Daan, C. Mojie, *Journal of Power Sources* (2009) 400–407.
- [67] T. Kato, S. Hayasaka, *Japanese Journal of Ophthalmology* 42 (1999) 461–465.
- [68] S. Valluru, *West Virginia University*, 2005.
- [69] X. Liu, C.L. Martin, D. Bouvard, S. Di Iorio, J. Laurencin, G. Delette, *Journal of the American Ceramic Society* 94 (2011) 3500–3508.
- [70] A. Atkinson, A. Selçuk, *Acta Materialia* 47 (1999) 867–874.
- [71] C.S. Montross, H. Yokokawa, M. Dokya, *British Ceramic Transactions* 101 (2002) 85–93.